

Master's Thesis

Academic year 2025

# Design and Control of the Lift Subsystem of a Two-Wheeled Forklift Robot

Sergio Esteban Quintero Benavides  
(Student ID No.: 82423418)

Supervisor: Professor Toshiyuki Murakami  
Co-supervisor: Professor Teresa Zielińska

September 2025

Keio University  
Graduate School of Science and Technology  
School of Integrated Design Engineering



## **Design and Control of the Lift Subsystem of a Two-Wheeled Forklift Robot**

**Abstract.** This thesis proposes the mechanical design and control of the lift subsystem of a Two-Wheeled Forklift Robot (TWFR). Vertical movement is achieved by employing a ball screw linear actuator that creates a movement of the fork relative to the main body of the robot. Vertical stabilization and trajectory generation of the robot are achieved by implementing a precise positioning of the Center of Gravity (CoG) of the complete system; this positioning considers the dynamic effects of changing the height of the load by the implementation of Reaction Torque Observers (RTOBs) and a special Inverse Kinematics (IK) solution that takes into account not only the position of the end effector but also the coordinates of the CoG. The low-level strategies for controlling pitch angle, fork angle, and lift height implement different disturbance observers and PD controllers to move the end effector and CoG to the desired position relative to the main axis of the wheels, allowing also a precise generation of the system trajectory. The performance of the trajectory generation and control strategies is tested in simulation to validate the proposed architecture.

**Keywords:** Two-Wheeled Robot (TWR), Mechanical design, Disturbance observer, Motion planning, Model-based control.



# Contents

<b>List of Figures</b> . . . . .	8
<b>List of Tables</b> . . . . .	8
<b>1 Literature review</b>	11
1.1 Stabilization Wheeled Doubled inverted pendulum . . . . .	11
1.2 Two-Wheeled Forklift Robot . . . . .	12
1.3 Two-wheeled manipulators . . . . .	12
1.4 Wheel-legged platforms . . . . .	14
1.5 Mobile manipulators . . . . .	16
1.6 Alternative platforms . . . . .	17
1.7 Conclusion . . . . .	18
<b>2 Objectives</b>	20
2.1 Background . . . . .	20
2.2 Research motivation . . . . .	20
2.3 Objectives . . . . .	21
<b>3 Approach and methodology</b>	22
<b>4 Lift mechanical design</b>	24
4.1 Actuator sizing . . . . .	24
4.2 CAD design . . . . .	24
4.2.1 Manual 3D modeling original robot . . . . .	24
4.2.2 Structural expansion . . . . .	26
4.2.3 Lift subassembly . . . . .	27
4.2.4 Fork subassembly . . . . .	29
4.2.5 Motion components . . . . .	29
4.2.6 Final considerations . . . . .	30
<b>5 Modeling</b>	31
5.1 Kinematics . . . . .	31
5.2 Dynamics . . . . .	34
5.2.1 Wheels . . . . .	34
5.2.2 Main body . . . . .	34

---

5.2.3	Lift . . . . .	35
5.2.4	Fork . . . . .	35
5.2.5	Euler-Lagrange equation . . . . .	35
5.2.6	Simplified dynamics . . . . .	38
<b>6</b>	<b>Control</b>	<b>40</b>
<b>6.1</b>	<b>Synthesized Pitch Angle Disturbance Observer (SPADO)</b> . . . . .	<b>40</b>
<b>6.2</b>	<b>Pitch Angle Control</b> . . . . .	<b>42</b>
<b>6.3</b>	<b>Fork Disturbance Observer (FDOB)</b> . . . . .	<b>42</b>
<b>6.4</b>	<b>Fork Angle Control</b> . . . . .	<b>43</b>
<b>6.5</b>	<b>Fork Reaction Torque Observer (FRTOB)</b> . . . . .	<b>43</b>
<b>6.6</b>	<b>Lift Disturbance Observer (LDOB)</b> . . . . .	<b>44</b>
<b>6.7</b>	<b>Lift Displacement Control</b> . . . . .	<b>46</b>
<b>6.8</b>	<b>Lift Reaction Force Observer (LRFOB)</b> . . . . .	<b>46</b>
<b>6.9</b>	<b>Wheel Position Control</b> . . . . .	<b>46</b>
<b>6.10</b>	<b>Control architecture</b> . . . . .	<b>47</b>
<b>6.11</b>	<b>Physical implementation</b> . . . . .	<b>47</b>
<b>7</b>	<b>Simulation results</b>	<b>49</b>
<b>7.1</b>	<b>Simulation parameters</b> . . . . .	<b>49</b>
<b>7.2</b>	<b>Proposed task</b> . . . . .	<b>50</b>
<b>7.3</b>	<b>Reference motion profiles</b> . . . . .	<b>51</b>
<b>7.4</b>	<b>Response along X-axis</b> . . . . .	<b>52</b>
<b>7.5</b>	<b>Response along Z-axis</b> . . . . .	<b>53</b>
<b>7.6</b>	<b>Parameter estimation of external load</b> . . . . .	<b>54</b>
<b>8</b>	<b>Discussion</b>	<b>56</b>
<b>8.1</b>	<b>Proposed task</b> . . . . .	<b>56</b>
<b>8.2</b>	<b>Reference motion profiles</b> . . . . .	<b>56</b>
<b>8.3</b>	<b>Motion response</b> . . . . .	<b>56</b>
<b>8.4</b>	<b>Parameter estimation</b> . . . . .	<b>57</b>
<b>8.5</b>	<b>Physical implementation</b> . . . . .	<b>57</b>
<b>9</b>	<b>Conclusions</b>	<b>58</b>

# List of Figures

1.1.1	<i>Two wheel mobile manipulator</i> [1] . . . . .	11
1.3.1	<i>Handle</i> by Boston Dynamics [5] . . . . .	13
1.3.2	<i>evoBot</i> by Fraunhofer Institute for Material Flow and Logistics IML [6] . . .	13
1.3.3	<i>Possible transitions between locomotion modes</i> [7] . . . . .	14
1.4.1	<i>Ascento</i> by Autonomous Systems Lab, ETH Zurich. [9] . . . . .	15
1.4.2	<i>Ollie</i> by Tencent Robotics. [11] . . . . .	15
1.5.1	<i>Mobile manipulator 2P7R</i> [13] . . . . .	16
1.6.1	<i>ANYmal</i> by Robotic Systems Lab, ETH Zürich. [16] . . . . .	18
1.6.2	<i>M4</i> by California Institute of Technology. a. Robot M4 in wheeled mode. b. Possible transformations of M4 to other modes.[18] . . . . .	18
4.1.1	ETH2-17 actuator characteristics [19]. . . . .	25
4.2.1	Original TWFR design. . . . .	25
4.2.2	Actual TWFR system. . . . .	26
4.2.3	Design of the new aluminum structural top plate. . . . .	26
4.2.4	Placement of new additional components over the new aluminum top plate. .	27
4.2.5	Manufactured new aluminum plate with the acquired actuator's driver and the 24V power source. . . . .	27
4.2.6	Actuator's base plate. . . . .	28
4.2.7	Linear actuator attached to its support plate. . . . .	28
4.2.8	Connection of the linear actuator with the main body of the TWFR. . . . .	28
4.2.9	Final assembly of the new TWFR. . . . .	29
4.2.10	Top plate to be attached to the mobile carriage of the actuator. . . . .	29
5.0.1	Abstraction model of the TWFR. . . . .	31
5.1.1	Kinematic diagram of the TWFR. . . . .	32
5.2.1	Simplified model of the TWFR. . . . .	38
6.1.1	Block diagram SPADO. . . . .	41
6.2.1	Block diagram SPADO-PD controller pitch angle. . . . .	42
6.3.1	Block diagram FDOB. . . . .	43
6.4.1	Block diagram FDOB-PD controller fork angle. . . . .	44
6.5.1	Block diagram FROTB. . . . .	45
6.6.1	Block diagram LDOB. . . . .	45
6.7.1	Block diagram LDOB-PD controller lift displacement. . . . .	46

6.8.1	Block diagram LRFOB. . . . .	47
6.10.1	Block diagram of the complete control architecture of the TWFR. . . . .	48
6.11.1	Hardware control architecture. . . . .	48
7.2.1	Model of TWFR in the simulation environment of MATLAB-Simulink. . . . .	50
7.3.1	Reference position, velocity, and acceleration profiles of the TWFR along the X coordinate. . . . .	51
7.3.2	Reference position and velocity of the TWFR's fork along the Z coordinate. .	51
7.4.1	Reference and response position of the TWFR along the X coordinate. . . . .	52
7.4.2	Position error of the TWFR along the X coordinate during the execution of the proposed task. . . . .	53
7.4.3	Reference S-shape profile and response velocity of the TWFR along the X coordinate. . . . .	53
7.5.1	Reference and response position of the fork along the Z coordinate. . . . .	54
7.5.2	Position error of the fork along the Z coordinate during the execution of the proposed task. . . . .	54
7.6.1	Estimated value of the torque caused by the external load of 5kg placed at 0.37m from the rotational axis of the fork (18.142Nm). . . . .	55
7.6.2	Estimated value of the mass of the external load (5kg). . . . .	55

## List of Tables

4.2.1	TWFR motion components . . . . .	30
5.0.1	Model parameters of the TWFR . . . . .	32
5.1.1	Modified DH parameters of the TWFR . . . . .	33
7.1.1	Experimental parameters . . . . .	49
7.3.1	Motion profiles parameters . . . . .	52

# Introduction

In modern industrial environments, humans and robots must work together "side by side". In several countries, there is a labor shortage due to the low birth rate that has been observed around the world in the last decades, creating, as a consequence, aging societies. In addition, robotic systems are employed to carry out tasks that involve health risks to human workers. In warehouses or assembly lines, the movement of load or material is a main task, which, executed repetitively by humans, could lead to future chronic physical problems. However, implementing mobile robotic systems must also guarantee the safety of the workspace. Considering these factors, a Two-Wheeled Forklift Robot (TWFR) is proposed to optimize the space occupied by the robot and reduce the impact force during a potential collision due to its compact design.

This work aims to propose the mechanical design and control of the lift subsystem of the Keio Murakami Laboratory TWFR. The mechanical design of the lift employs a modular approach, offering flexibility in the distribution of mass within the main body of the robot. For that reason, a ball screw linear actuator is proposed for the vertical movement of the fork; this particular mechanism offers high accuracy, repeatability, and maximum payload, important features for this particular application. The system's control is achieved by the implementation of different disturbance observers and PD controllers in the different subsystems of the robot. It is proposed that the Synthesized Pitch Angle Disturbance Observer (SPADO) be used to model the unified disturbances that affect the wheels' angle and the robot's pitch angle. It is important to have this synthesized disturbance observer because of the underactuated condition of the system.

The dynamics of Two-Wheeled Robots (TWR) depend on the position of their Center of Gravity (CoG); thus, the position of the CoG not only stabilizes the system but also drives its trajectory, for that reason, the position of the end effector and the CoG should be considered in an unified Inverse Kinematics (IK) solution, common in loco-manipulation platforms. This particular solution must also take into account the effects of the external load on the position of the CoG, which is why different Reaction Torque Observers (RTOBs) are used to estimate the external load placed over the fork and change the reference CoG position accordingly. The controller for the rotational joint of the fork uses a disturbance observer to compensate for the effects of the external load and the internal residual torques. The position control of the fork is done by a PD controller that makes

sure the fork is parallel to the ground when the external load is placed on it.

The same previously discussed control architecture for the lift subsystem is proposed. A disturbance observer is used to compensate for the external and internal forces that affect the mechanism, and a PD controller regulates the linear movement of the lift to move the load vertically to the desired height. The experiments confirmed the capability of the system to achieve the desired vertical movement of the load and the possibility of estimating the weight of the external load by implementing a RTOB that considers only the linear movement of the lift.

This work aims to propose the mechanical design and control for the lift subsystem of an existing TWFR. The design of the lift is discussed in Chapter 4, the mathematical model of the robot including the new linear subsystem and the effects of the position of the CoG on the trajectory of the robot is presented in Chapter 5, the control of the robot is discussed in Chapter 6 where a PD controller and a disturbance observer is proposed to control the vertical displacement of the lift, furthermore, it presents how RTOB implemented on the fork and lift sysbsystems are used to estimate the weight and position of the external load over the fork. Chapter 7 presents the simulation results of the proposed controller, and Chapter 8 provides a deeper discussion about the obtained results, considering the implementation of a simple motion task that demonstrates the performance of the integrated system. Finally, this work presents in Chapter 9 the conclusions of the presented thesis and the future work.

# Chapter 1

## Literature review

### 1.1 Stabilization Wheeled Doubled inverted pendulum

In [1], the authors considered the stabilization control of a four-link inverted pendulum over a two-wheeled mobile base as the one shown in Figure 1.1.1. For such a task, a second-order sliding mode controller (SMC) is proposed over a simplified double inverted pendulum model of the robot. This controller aims to reduce the natural chattering of SMC by increasing the order of the controller and decreasing the uncertainty and disturbance effects over the model of the robot with a disturbance observer. This controller was proven to have better performance than a conventional PD strategy, mainly in the reduction of the movement of the arm joints and the position response. It is important to mention that this work shows how this kind of controller depends on the correct estimation of the internal parameters of the robot and the necessity of additional observers to reduce the uncertainty that could produce stabilization problems over the system.



**Figure 1.1.1.** Two wheel mobile manipulator [1]

Following the line of different solutions for the stabilization problem of a double inverted pendulum over a two-wheeled robot, the authors in [2] present the use of an

H-infinity controller and its comparison with the well-known LQR controller. H-infinity controllers are considered robust controllers, making them very suitable for nonlinear systems subjected to considerable external disturbances. In this work, it is proved that the proposed controller is not only capable of stabilizing the system but also shows a better performance than the LQR controller, in the stabilization time and position error with respect to the reference value.

## 1.2 Two-Wheeled Forklift Robot

The control of the Two-Wheeled Forklift Robot (TWFR) has been discussed in several papers relevant to the current research. In [3], the authors propose a model predictive controller over a TWFR that consists of a fork placed on top of the main body of the robot with one rotational joint; thus, the system is modeled as a double inverted pendulum. In this approach, it is intended to control the position and pitch angle of the robot using a model-based predictive functional control. The internal model of the robot is corrected using a synthesized pitch angle disturbance observer (SPADO), this observer reduces the error induced by the disturbances over the pitch angle of the robot. It is important to notice that this controller was tested in simulation, considering only the linear position of the robot and its pitch angle, and keeping the arm parallel to the ground.

Similarly to the previous work, [4] considers a TWFR with a similar configuration and uses a SPADO to counterpose the estimation error of the pitch angle in the model of the robot, in this case, the control strategy seeks to reduce the movement of the wheels of a TWFR when a load is placed over the arm. This goal is achieved by compensating the pitch angle due to a change in the CoG of the system produced by the placement and removal of the load. The compensation of the CoG uses a reaction torque observer (RTOB) that estimates the torque applied by the external load to the arm. In addition to that, the pitch angle and wheel position controllers use PD and PI control strategies, respectively, to stabilize the system after the application of the external load.

## 1.3 Two-wheeled manipulators

One of the most advanced two-wheeled robots with a manipulator arm known to date, this document is written is the *Handle* robot created by Boston Dynamics [5]. This two-wheeled-legged robot is capable of executing pick and place tasks of boxes in a warehouse environment. No further information has been provided by this specific system, and most of the information comes from videos and technical blogs describing its general capabilities. In particular, this robot has a 4 degrees of freedom (DoF) arm that allows it to manipulate objects from the environment. For the stabilization and manipulation

tasks, the robot uses an active counterbalance system that balances the effects produced by external torques and the change of the center of gravity (CoG) of the robot.



**Figure 1.3.1.** *Handle* by Boston Dynamics [5]

On the other hand, the Fraunhofer Institute with its robot *evoBOT* [6] shows an interesting two-wheeled system capable of changing its configuration to execute manipulation tasks or to perform different locomotion modes. The system can be described as a double inverted pendulum with an active joint between the two links of the pendulum. The control techniques and further technical characteristics are not openly available; nevertheless, they show an important improvement in two-wheeled manipulators.



**Figure 1.3.2.** *evoBot* by Fraunhofer Institute for Material Flow and Logistics IML [6]

As it is proposed in [7], some systems include the possibility of several locomotion modes to gain stability for manipulation purposes. In particular, in this work, the authors develop a force control method to change from a two-wheeled mode to a four-wheeled locomotion mode that makes the system more stable for manipulation tasks, as is demonstrated in Figure 1.3.3. Although it loses the flexibility offered by the original two-wheeled

configuration. Nevertheless, this approach gives an interesting point of view in such as it is possible to decouple the locomotion and manipulation modes, changing the standing modes of the robot.

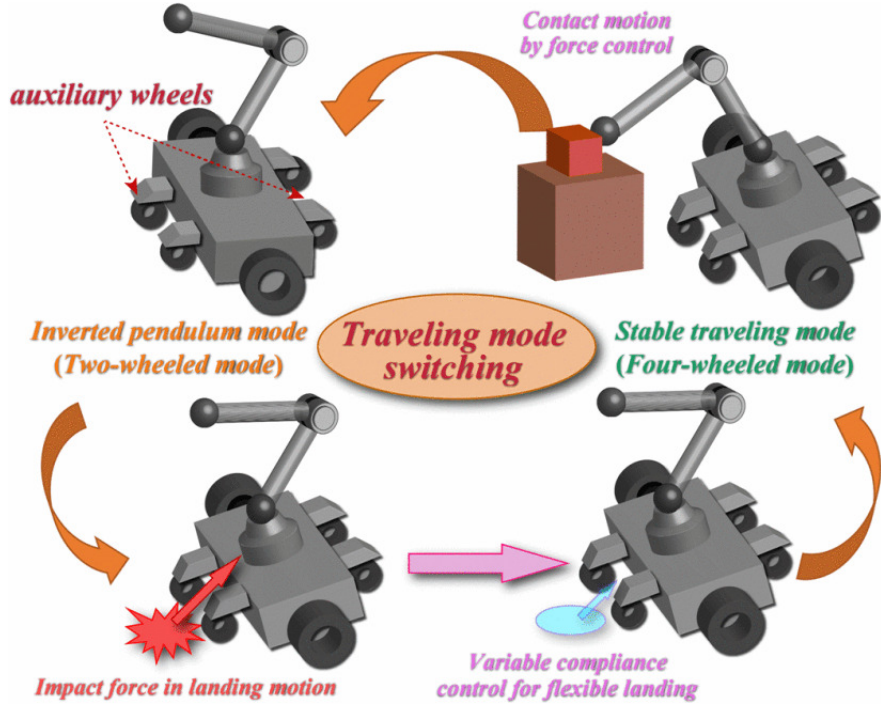


**Figure 1.3.3.** Possible transitions between locomotion modes [7]

Two-wheeled mobile robots (TWMRs) and their use in load handling and manipulation applications represent a control challenge due to the highly unstable dynamic behavior of such systems and the variability of their model parameters that this particular application introduces. Considering the change of the model parameters introduced by an external load that will be manipulated by the system, [8] proposes a Gain Scheduled LQR controller that triggers different LQR gains based on the different possible operating points of the system. That is because this particular system cannot be properly regulated with a single gain LQR controller. However, this approach requires a previous calculation of the possible LQR gains changing the length and mass of the inverted pendulum that limits the range of the possible inertia changes of the system.

## 1.4 Wheel-legged platforms

Over the years, different designs of two-wheeled robots have been proposed to improve their versatility and application range. Examples of these alternative approaches are the two-wheel-legged robots that combine the locomotion advantages that bipedal robots and wheeled robots provide. In [9], the two-wheeled legged robotic platform *Ascento* is presented. This system uses different controllers to achieve distinct capabilities such as

stabilization, jumping, and fall recovery. The stabilization of the robot is achieved with a model-based LQR controller. For the jumping task, the authors proposed PID control strategies for different stages of the task until the robot lands on the floor, returning to the initial LQR controller.



**Figure 1.4.1.** *Ascento* by Autonomous Systems Lab, ETH Zurich. [9]

Alternatively, [10] presents a different control system for the wheel-legged robot *Ollie* [11]. In this work, the authors present a system with a planar parallel mechanism for the legs, improving in that way the flexibility of the robot. For the stabilization task, an LQR controller is proposed to keep the balance of the robot in a standstill position. However, an interesting nonlinear control strategy called interconnection and damping assignment-passivity-based control (IDA-PBC) is used to control the position of the robot when the initial pitch angle is far from the equilibrium point, and to change the height of the robot while it is moving. Finally, the authors manifest the intention to attach a manipulator to the presented platform; nevertheless, no further research on this idea has been published by the date when the current state of the art is written.



**Figure 1.4.2.** *Ollie* by Tencent Robotics. [11]

Considering a two-wheel-legged robot with an arm, the focus of research is mainly on manipulation tasks. Nevertheless, [12] proposes the use of an arm over a two-wheel-legged

robot as a stabilizer for locomotion tasks. In this work, the main idea is that the change in the acceleration and position of the end-effector of the arm could reduce the disturbances over the entire system during the execution of different locomotion tasks, because the modeling and control of the base platform and the arm are decoupled. In particular, the wheel-legged platform is controlled with an LQR controller for vertical stabilization, and the arm uses a PD controller for the acceleration and position velocity of the end-effector. In such a control scheme, the arm is activated if the acceleration of the torso of the robot is greater than a certain threshold or if the intended trajectory of the center of gravity has a pronounced curve.

## 1.5 Mobile manipulators

In general, the study of manipulator arms over mobile platforms represents a wide and important field of study because of its different applications. In [13], a method to solve the inverse kinematics of a 9 DoF mobile manipulator is presented. In this particular system, a 6 DoF arm is mounted over a holonomic mobile platform modeled as a system with two prismatic joints and one rotational joint, constituting in that way a 2P7R redundant robot. In this work, the differential evolution (DE) algorithm is used to solve the inverse kinematics problem. The proposed numerical method showed a smaller end-effector position error compared with the classical PSO algorithm. In that way, DE could be an interesting approach to solve future inverse kinematic problems over two-wheeled manipulator robots with a very stable base.

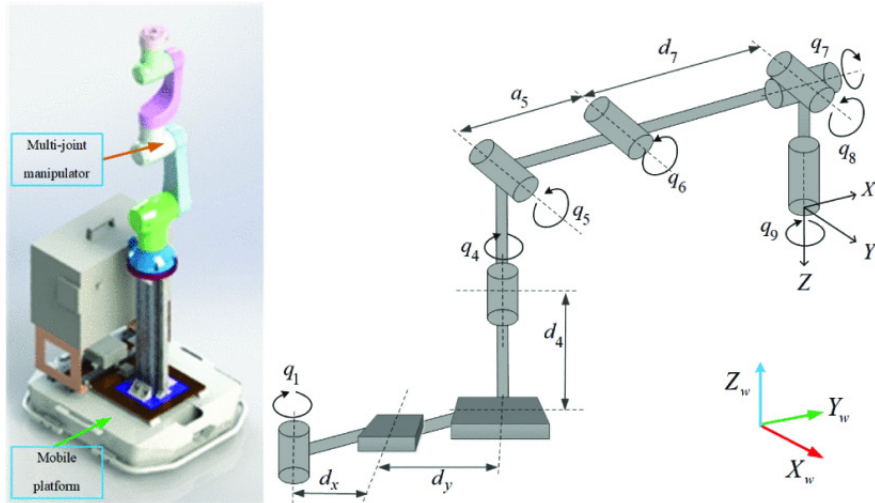


**Figure 1.5.1. Mobile manipulator 2P7R [13]**

In [14], a computed torque control (CTC) strategy is proposed over a non-holonomic differential robot with a 3 DoF manipulator. This nonlinear controller follows a model-based approach that considerably differs from the usual two-wheeled robot models. Nevertheless, this particular controller shows good performance in the presence of external

torques, which is interesting when it is considered that the robot should be able to manipulate external objects that are also modeled as external torques.

Most of the above-mentioned algorithms require a complete knowledge of the model of the robot; despite that, [15] shows a neural-network-based control (NNBC) algorithm that is independent of the mathematical model of the robot. In this paper, the authors use a zeroing neural network to track the end effector reference of a robotic arm over a mobile platform. Additionally, an estimation of the Jacobian of the robot is performed with another neural network to find a solution to the inverse kinematics of the robot. This method has proved to solve the accumulation of the error produced by the uncertainty of the real values of the different internal parameters of the robot. Nevertheless, it is necessary to have an initial relation between the base frame of the manipulator and the mobile base. In this particular experiment, the base mobile platform is assumed as a regular non-holonomic mobile robot without variation in its pitch angle. As the NNBC does not require previous knowledge of the robot, it could be suitable for a two-wheeled mobile robot.

## 1.6 Alternative platforms

The robotic platform presented in [16] and [17] can change between different locomotion modes to execute different manipulation tasks when the robot is in a two-wheeled configuration. In [16], the authors used a Reinforcement Learning (RL) approach to teach the robot how to change from a four-wheeled to a two-wheeled configuration. The particular technique used is called Multiple Adversarial Motion Priors (MAMP). This algorithm is mainly used in the computer graphics field, and it encodes motion data from a previous reference data set, rewarding the most interesting poses and movements.

On the other hand, [17] presents the same robotic platform executing manipulation tasks as picking a package and opening a door, while it keeps balanced on two wheels. The shown manipulation skills were achieved again using an RL approach called Curiosity-Driven Learning. It is important to mention that part of the experiments of this work were done with the real robot, which provides relevant advances for two-wheeled systems executing Loco-manipulation tasks.

Another interesting platform that uses two-wheeled locomotion is the hybrid bio-inspired robot M4 presented in [18]. This robot has different terrestrial and aerial locomotion modes. The proposed platform can transform the propulsion modules for aerial locomotion into wheels for terrestrial locomotion. One of the achievable terrestrial locomotion modes of the robot is the two-wheeled locomotion, which is used mainly to overcome obstacles and to climb inclined slopes. Thus, the robot is capable of standing up using a pair of propellers, and when it reaches a stable vertical zone, it switches to the conventional two-wheeled locomotion. Analogously, to climb slopes with a considerable



**Figure 1.6.1.** ANYmal by Robotic Systems Lab, ETH Zürich. [16]

angle, the robot uses two of its propellers to propel itself along the plane, moving the other two wheels, achieving a hybrid two-wheeled locomotion.

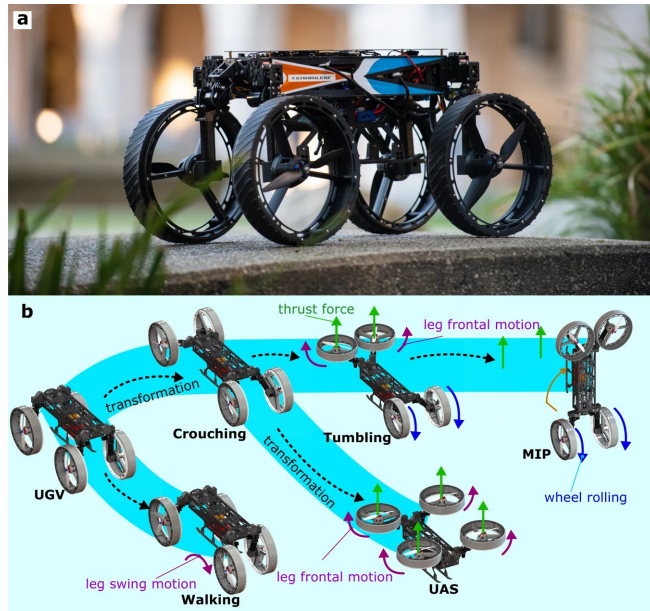


**Figure 1.6.2.** M4 by California Institute of Technology. a. Robot M4 in wheeled mode. b. Possible transformations of M4 to other modes.[18]

## 1.7 Conclusion

The above-presented state-of-the-art showcases the most recent control techniques applied to various two-wheeled robotic platforms. The fundamental control techniques that are used as a reference for the self-balance problem are PID controllers complemented with disturbance observers and LQR controllers. These particular controllers have been tested several times in simulation and real robots, showing an adequate performance in

simple locomotion and manipulation scenarios. Furthermore, many research laboratories implement these control techniques in hybrid implementations as two-wheeled legged robots.

Nevertheless, for more complex systems as robotic platforms with several locomotion modes, the use of Machine Learning (ML) approaches, to include manipulation tasks, starts to be more recurrent to make the controller independent of the complete knowledge of the system. Thus, two main approaches have been identified to make a robotic platform able to execute loco-manipulation tasks. The first one is solving locomotion and manipulation tasks using model-based control techniques, and the second one uses ML approaches to consider a more general solution.

# **Chapter 2**

## **Objectives**

### **2.1 Background**

The present research is conducted as part of the Two-Wheeled Forklift Robot (TWFR) project at Murakami Laboratory, in collaboration with Toyota Industries Corporation. This project aims to develop various control strategies for such systems, enabling their deployment in industrial environments where robots and humans collaborate under space-constrained conditions. Currently, Murakami Laboratory has a TWFR that consists of a fork with a single rotational joint and a maximum payload of ten kilograms. Because of the interest in increasing the current functionality of the robot, this thesis aims to provide new ideas and perspectives in the use of Two-Wheeled robots as loco-manipulation capable devices with a simple, model-based control architecture for specific manipulation tasks, compared with complex humanoid-like robots mainly used for general-purpose tasks. This perspective reduces the technical requirements for the implementation of the control strategies in hardware and software, making this solution very attractive for industrial environments.

### **2.2 Research motivation**

In recent decades, many industrialized countries have experienced declining birth rates, leading to projected mid- and long-term labor shortages across various industries. In an industrial context, this challenge can be addressed technologically by developing robotic systems designed to work alongside humans. Such systems not only help offset labor shortages but can also perform tasks that pose health risks to human workers. For example, in assembly lines, workers often need to move objects repeatedly from one station to another. While this task may not be especially demanding in the short term, performing it continuously over long periods can reduce productivity and cause mild physical issues. Implementing a mid-range, mid-payload industrial vehicle to handle material transport offers a practical and effective solution to this problem.

The implementation of mobile robots in industrial environments requires specific design considerations to maintain the safety of human workers and optimize the available space. With those constraints in mind, the conception of a Two-Wheeled Robot is reasonable because of its small footprint and compact design, allowing it to be implemented in spaces that are already suitable for human workers. Additionally, the dynamic behavior of this system allows it to reduce the impact force caused by possible collisions with the environment. Considering that it is not required that the system has high manipulability capabilities, the motion planning and control of the robot can be done using classical model-based techniques, simplifying the physical implementation of the robot.

## 2.3 Objectives

Due to the need to expand the working space of the current system, the primary objective of this thesis is to design a lift subsystem for the TWFR and develop the relevant control strategies for executing loco-manipulation tasks. This additional feature will allow the robot to load and release objects at different heights, improving its functionality and versatility for different industrial scenarios. As this system is designed to work in industrial environments, it is important to develop a reliable control strategy that ensures safety and functionality. For those reasons, a model-based control approach will be used in this work because of its simple design, predictability, and robustness compared to learning approaches in this specific system.

# Chapter 3

## Approach and methodology

Following the requirements provided by Toyota Industries Corporation, the new subsystem was designed to avoid significantly changing the main structure of the existing robot. To achieve this, an initial CAD model of the current system was created using *Autodesk Inventor*. This modeling process involved manually measuring the robot's external structure and identifying the commercial components in use, such as gearboxes, motors, and motor drivers.

Once the initial 3D model was complete and the components were identified, it became possible to select an appropriate linear actuator for the lift subsystem. Actuator sizing was carried out based on the desired payload and the physical properties of the fork subsystem. At this stage, particular attention was paid to how the additional linear actuator would affect the robot's inertia and, consequently, how the mathematical model would need to change to support the design of the motion controllers. With the actuator selected, the interfaces between the main system and the new subsystem were designed, taking into account the robot's mass distribution to ensure balance and facilitate control design.

This thesis focuses on the robot's motion in a single horizontal axis for locomotion tasks, and in the vertical axis for the forklift's end effector. For this reason, the system is designed to execute motion tasks in both axes simultaneously. The extended robot was modeled mathematically, incorporating the physical constraints introduced by the new subsystem. Given the additional degree of freedom, it was necessary to develop a motion planning system and a control system capable of coordinating motion in these two principal axes. This required creating both a kinematic and a dynamic model of the robot to provide the necessary equations for the motion planner and controller.

The motion planner uses the system's kinematic model to determine joint positions relative to the robot's base, achieving the desired motion in the Z-axis while also following CoG position references for horizontal motion control. The locomotion task relies on

this kinematic solution as well as on a simplified dynamic model that relates the desired horizontal motion profile to the robot's CoG position. Based on the reference joint values generated by the motion planner, each subsystem's low-level controller was designed using the complete dynamic model. These controllers use a combination of PD torque controllers and disturbance observers to enhance robustness against external disturbances and unmodeled dynamics.

The motion trajectories were designed using S-shaped and trapezoidal velocity profiles. To track the desired horizontal position reference, an additional PD controller was implemented to add a closed-loop trajectory tracking to the system. This controller relates the desired position to the reference pitch angle of the robot's main body. The performance of the designed motion planner and controller was evaluated in *MATLAB* and *Simulink*, using the Simscape library to model the physical mechanical system. The simulation's physical properties were derived from the specifications provided in the component catalogs.

The manufacturing of the designed mechanical parts was carried out at the *Manufacturing Center of Keio University*. Most components were manufactured in aluminum to minimize weight while maintaining sufficient rigidity during movement and load handling. Additionally, L-shaped brackets were used to provide stability to the assembly without requiring extra custom-designed components.

The controller was physically implemented using an industrial computer (IPC) from *Beckhoff Automation*, which communicates with the motor drivers and IMU sensor via the *EtherCAT* protocol. The controller was designed and programmed in *Simulink*, then deployed to the IPC through C code generation. This programming process was performed on an external general-purpose PC, which also recorded the data collected during physical experiments.

# **Chapter 4**

## **Lift mechanical design**

### **4.1 Actuator sizing**

The main design idea consists of placing in the back of the current robot a linear actuator that lifts the fork subassembly and, in consequence, the external load. The sizing of the required linear actuator was done taking into account the weight of the base plate, the fork mechanism, and the maximum payload. The current work proposes the implementation of a ball screw linear actuator due to its load capability, repeatability, easy installation, and low cost compared to belt-driven or hydraulic actuators. Considering that the external load will be moved between shelves that have less than 0.9m height, a stroke of 350mm was chosen for the actuator. Given the weight of the fork subassembly, which is around 21.5kg, and the maximum payload of 10kg, it is desired to consider the linear actuator's maximum vertical payload of 40kg. Additionally, it was considered that the desired application motion profiles do not exceed 150mm/s for the velocity and 100mm/s<sup>2</sup> for the acceleration limits. With those design constraints, the Ball Screw Linear Actuator ETH2-17-L5-350-BC-M40B-C6N5L-FF19 from the company *TOYO Robotics* was chosen. Figure 4.1.1 shows the technical specifications of the linear actuator based on the manufacturer's datasheet [19]. Given that the maximum linear speed is 300mm/s, and the maximum acceleration is 0.15g or 1.47m/s<sup>2</sup>, this actuator is suitable for the desired application. Additionally, it was desired to include an external electromagnetic brake unit for safety reasons in case of a sudden power failure. This unit requires the addition of an external 24V power source that will be included in the main structure of the system.

### **4.2 CAD design**

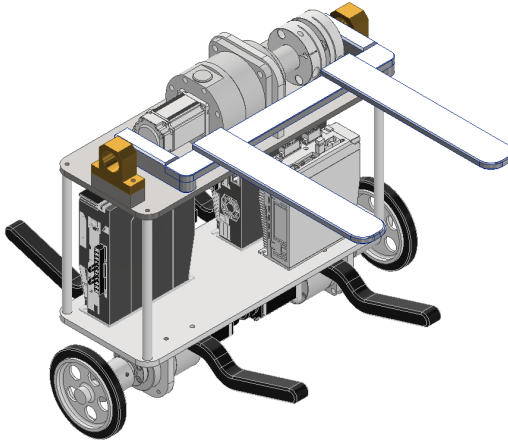
#### **4.2.1 Manual 3D modeling original robot**

The chosen actuator uses the Mitsubishi servomotor HG-KR43B with the MR-J4-40TM-ECT driver. This servomotor has an electromagnetic brake that requires the use of an external DC source. These additional components, the servo driver and the DC power

		(+/−0.005)				
	mm	5	10	20	40	
Lead	rpm	3600	3600	3600	3600	
Maximum Rotating Speed(mm/s)	mm/s	300	600	1200	2400	
Maximum Linear Speed						
	Horizontal	kg	120	110	75	16
Maximum Payload	Vertical (For Non-generative power)	kg	40	25	11	9
	Vertical(external 50W regenerative resistor)	Kg	50	30	18	15
Rated Thrust	N	1389	694	347	174	
Stroke Pitch	mm	50-1200mm/50 intervals(50mm pitch)				
Maximum Acceleration	G	0.15	0.31	0.61	1.22	
Ball Screw	Basic Dynamic load rating Ca	N	13428	11223	5667	9656
	Basic Static load rating Coa	N	29671	24456	11182	20274
Linear Guide	Dynamic Horizontal	N	7866			
	Static Horizontal	N	78400			
Fixed Bearing	Basic Dynamic load rating Cr	N	9666			
	Static Load rating Cor	N	6400			
AC Actuator with Motor Output	W	400				
Ball Screw	mm	C7 X ±20				
Linear Guide	mm	W150X12.5				
Ball Screw	mm	14 X 12				
Home Sensor	Outside	T64N2(NPN)				

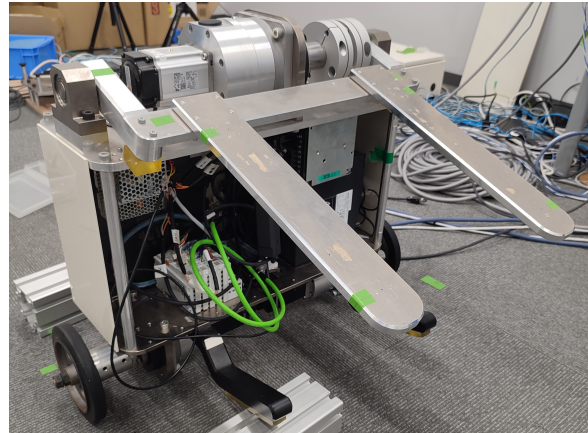
**Figure 4.1.1.** ETH2-17 actuator characteristics [19].

source, must be placed in the main body of the robot. Changing the width and depth of the robot to create more space would require a complete redesign of the main external structure; for that reason, the new system design increases the height of the robot to make space for the new components. Figure 4.2.1 presents the original design of the TWFR of Murakami Laboratory. This CAD model was made from scratch, measuring manually all the structural components of the actual robot and using the available CAD models of the commercially available gearboxes, servomotors, and motor drivers.



**Figure 4.2.1.** Original TWFR design.

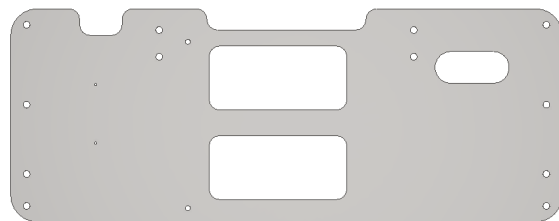
The actual system and its real distribution of internal components are exposed in Figure 4.2.2. It is possible to see that the system has other internal elements than the ones shown in the ideal CAD design, such as power sources, cables, and connectors. It is important to mention that these components do not play an important role in the development of the presented CAD model. However, they are relevant for the dynamics of the system, not necessarily because of their weight but because of their distribution in the robot's body and thus their impact on its inertia.



**Figure 4.2.2.** Actual TWFR system.

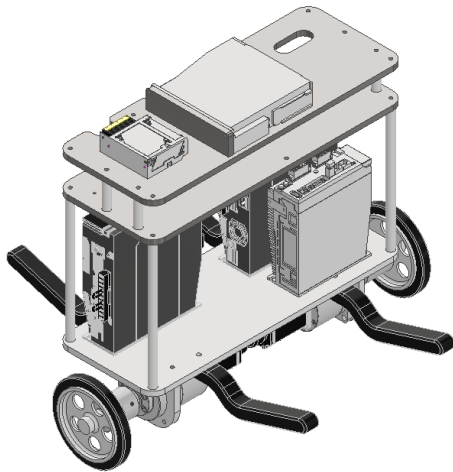
#### 4.2.2 Structural expansion

To increase the height of the robot and avoid changes in the structure of the original top plate, a new aluminum plate was placed on top of four structural bars located in the original position of the pillow blocks of the fork subassembly. The design of this plate takes into account the space required to avoid contact with the new components that will compose the new lift subassembly, and also considers a way for the cables to go from one section of the body to the other for the required electrical connections. This is achieved by the implementation of slots on the edges and in the area of the plate. Additionally, wide rectangular cuts were done in the middle of the plate to provide the proper refrigeration for the linear actuator's servo-driver because it is supposed to be placed horizontally to keep the height of the new robot as low as possible. Figure 4.2.3 shows the designed plate with the mentioned functional features.



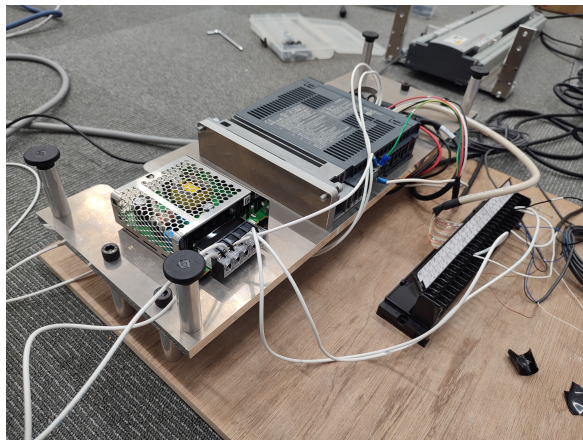
**Figure 4.2.3.** Design of the new aluminum structural top plate.

Figure 4.2.4 depicts the placement of the plate on top of the original robot's body. As can be appreciated, the new plate provides more space to place the servo-driver, and the additional power source for the electromagnetic brake, keeping the internal distribution of the main robot's body in its original configuration. An additional structural plate was added to properly secure the servo-driver to the base plate. Further changes must be made to the electrical connections of all the systems; nevertheless, these changes do not represent a relevant structural change, keeping the initial non-invasive structural changes requirements.



**Figure 4.2.4.** Placement of new additional components over the new aluminum top plate.

In Figure 4.2.5, the proposed manufactured subassembly is shown. Over the designed base plate, the servo-driver and the required 24V power source were already placed and secured. The servo-driver is assembled using the mentioned structural plate to couple its original mechanical connection interface.



**Figure 4.2.5.** Manufactured new aluminum plate with the acquired actuator's driver and the 24V power source.

### 4.2.3 Lift subassembly

The linear actuator is attached to the main body of the robot by the above described new top plate using three structural aluminum plates and L-shaped stainless steel brackets to guarantee rigidity in the connection. Figure 4.2.6 depicts the main base plate that is positioned behind the linear actuator to be attached afterwards to the robot's main body.

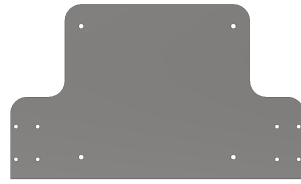


**Figure 4.2.6.** Actuator's base plate.

The acquired linear actuator is displayed in Figure 4.2.7. It can be seen that the actuator is assembled to its base plate, which is also attached to two additional plates that will be assembled with the body's top plate, previously shown.



**Figure 4.2.7.** Linear actuator attached to its support plate.

This structural assembly is important because all the load that the lift will move is transmitted to the main body of the robot through this structure, which is why it is important to have a stable mechanical connection. All these structural components are assembled between each other by stainless steel bolts. Figure 4.2.8 illustrates the placement of the linear actuator over the main body of the robot.

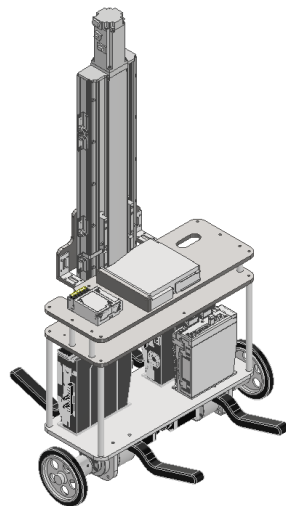


**Figure 4.2.8.** Connection of the linear actuator with the main body of the TWFR.

#### 4.2.4 Fork subassembly

Finally, the fork subassembly is placed over an aluminum base plate that is attached to the mobile carriage of the actuator. Additionally, four steel bars with plastic supports are placed on the corners of the new top plate that will be used as a mechanical base when the lift is in its lowest height, as depicted in Figure 4.2.9. This illustration also exposes the robot at the highest possible height of the lift. In case of a sudden power failure, the linear actuator's brake will activate, avoiding the fork subassembly and the load from falling over the main body of the robot.

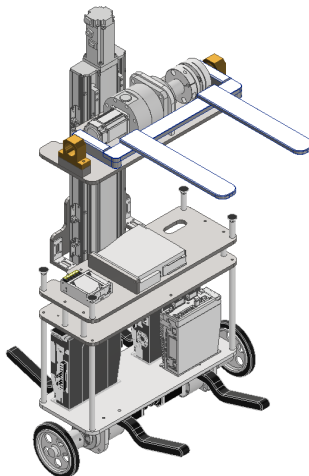


**Figure 4.2.9.** Final assembly of the new TWFR.

Figure 4.2.10 shows the manufactured top plate where the fork subassembly will be attached, and that is used as a connection interface between the fork and lift subsystems.



**Figure 4.2.10.** Top plate to be attached to the mobile carriage of the actuator.

#### 4.2.5 Motion components

Besides the customized parts, it is relevant to describe the main motion components present on the TWFR, the list of components that includes the servomotors, reduction drives and drivers is presented in Table 4.2.1.

**Table 4.2.1.** TWFR motion components

Element	Reference	Manufacturer
Wheel motors	R88M-1M40030S-S2	OMRON
Wheel reduction drives	HPG-20A-11-J6GDK	HARMONIC DRIVE
Wheels motor drivers	R88D-1SN04L-ECT	OMRON
Fork motor	R88M-K40030S	OMRON
Fork reduction drive	HPG-32A-33-J2NELA	HARMONIC DRIVE
Fork motor driver	R88D-KN04L-ECT	OMRON
Lift motor	HG-KR43B	mitsubishi
Lift mechanism	ETH2-17-L5-350	TOYO ROBOTICS
Lift motor driver	MR-J4-40TM-ECT	mitsubishi

These elements were included in the CAD design to have geometric reference of the space that they occupy and their distribution in the main body of the robot. The CAD models of the components were downloaded freely from the official web-site of each manufacturer.

#### 4.2.6 Final considerations

The complete assembly of the system is not presented due to problems acquiring the proper servo-driver for the linear actuator. The servo-driver presented in Figure 4.2.5 is the default Mitsubishi driver MR-J4-40A that came with the linear actuator, but it is not compatible with the EtherCAT protocol, which is the main communication protocol for the control of the TWFR. The proper servo-driver MR-J4-40TM-ECT eventually arrived, but it was too late to complete the assembly and show the final result in this document. Additionally, it was impractical to assemble the complete system with the wrong driver because the TWFR is used by other students in its original configuration, and repetitive changes in the robot structure could also affect their work.

# Chapter 5

## Modeling

The mathematical modeling of the TWFR is based on the scheme presented in Figure 5.0.1 and the parameters described in Table 5.0.1. Taking into account that the main function of the robot is to move an external load that is placed over the fork, the orientation of the end effector must remain as constant as possible, parallel to the floor, to avoid dropping the object during the execution of the locomotion and lifting tasks. This condition implies that  $\theta_p + \theta_a = 0$  for the system's steady state; this expression will be used throughout this section to simplify the presented equations.

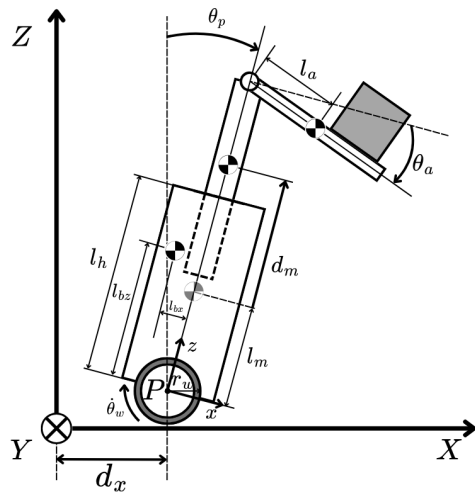


**Figure 5.0.1.** Abstraction model of the TWFR.

### 5.1 Kinematics

The kinematic diagram presented in Figure 5.1.1 models the TWFR as an RPR manipulator. Table 5.1.1 presents the modified Denavit-Hartenberg (DH) parameters of the robot.

The direct kinematics of the main kinematic chain can be expressed by the homogeneous transformation (5.1) obtained by the DH parameters and the assumption of

**Table 5.0.1.** Model parameters of the TWFR

Parameter	Explanation	Parameter	Explanation
$\theta_w$	Wheels angle	$m_b$	Body mass
$\theta_p$	Pitch angle	$m_m$	Lift mass
$d_m$	Lift displacement	$m_a$	Arm mass
$\theta_a$	Arm angle	$m_l$	External load mass
$l_{bx}$	Body CoG x coordinate	$t_l$	External load torque
$l_{bz}$	Body CoG z coordinate	$\tau_w$	Wheels torque
$l_m$	Lift CoG distance	$f_m$	Lift force
$l_h$	Body length	$\tau_a$	Arm torque
$l_a$	Arm CoG distance		

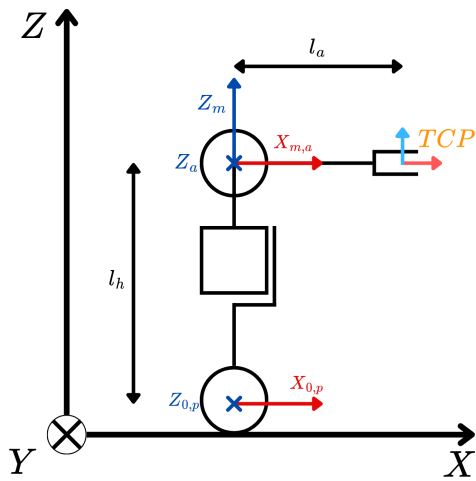


**Figure 5.1.1.** Kinematic diagram of the TWFR.

parallelism of the fork and the floor. In the following expressions  $s_o$  and  $c_o$  represent  $\sin(\theta_o)$  and  $\cos(\theta_o)$ .

$$H_3^0 = \begin{pmatrix} 1 & 0 & 0 & s_p(l_h + d_m) \\ 0 & 1 & 0 & -c_p(l_h + d_m) \\ 0 & 0 & 1 & 0 \\ 0 & 0 & 0 & 1 \end{pmatrix} \quad (5.1)$$

However, this expression does not relate the position of the end-effector and the world reference frame; thus, it is necessary to multiply the matrices that relate the homogeneous transformation of the kinematic chain with the reference frame and the TCP frame as follows.

$$H_T^B = H_0^B * H_3^0 * H_T^3 \quad (5.2)$$

Where,

**Table 5.1.1.** Modified DH parameters of the TWFR

j	$\theta_j$	$d_j$	$a_j$	$\alpha_j$	offset
1	$q_1$	0	0	0	0
2	0	$q_2$	0	$\pi/2$	$l_h$
3	$q_3$	0	0	$-\pi/2$	0

$$H_0^B = \begin{pmatrix} 1 & 0 & 0 & 0 \\ 0 & 0 & 1 & 0 \\ 0 & -1 & 0 & r_w \\ 0 & 0 & 0 & 1 \end{pmatrix} \quad H_T^3 = \begin{pmatrix} 1 & 0 & 0 & dt \\ 0 & 0 & -1 & 0 \\ 0 & 1 & 0 & 0 \\ 0 & 0 & 0 & 1 \end{pmatrix} \quad (5.3)$$

Finally, the direct kinematics of the TWFR is expressed by (5.4).

$$H_T^B = \begin{pmatrix} 1 & 0 & 0 & s_p(l_h + d_m) + l_a \\ 0 & 1 & 0 & 0 \\ 0 & 0 & 1 & r_w + c_p(l_h + d_m) \\ 0 & 0 & 0 & 1 \end{pmatrix} \quad (5.4)$$

Additionally, due to the necessity of creating a motion planner for the CoG, it is necessary to include its mathematical representation (5.5) in the kinematic equations.

$$CoG = \left( \frac{\frac{m_l(d_m s_p + l_h s_p + \frac{t_l}{g m_l}) + m_a(l_a + d_m s_p + l_h s_p) + m_b(l_{bz} s_p - l_{bx} c_p) + m_m(d_m + l_m)s_p}{m_a + m_b + m_l + m_m}}{\frac{(m_a + m_l)(d_m c_p + l_h c_p) + m_b(l_{bz} c_p + l_{bx} s_p) + m_m(d_m + l_m)c_p}{m_a + m_b + m_l + m_m}} \right) \quad (5.5)$$

The terms  $m_l$  and  $t_l$  correspond to the estimated mass and generated torque of the load placed over the fork, respectively. To achieve the desired behavior of the system, the Z position of the end effector and the X coordinate of the CoG are the expressions of interest to manipulate the load and obtain a desired trajectory profile. Additionally, to use designed velocity profiles for the motion planning, it is important to consider the differential kinematics of the robot. Given that the motion of the CoG is small because of the main task of keeping the robot stable vertically, it is possible to assume that  $\dot{CoG}_x = 0$ . Thus, the relevant kinematic expressions of the TWFR for motion planning are presented in (5.6).

$$\begin{cases} z^{ref} = r_w + c_p(l_h + d_m) \\ \dot{z}^{ref} = c_p \dot{d}_m - s_p(l_h + d_m)\dot{\theta}_p \\ CoG_x^{ref} = \frac{m_l(d_m s_p + l_h s_p + \frac{l_1}{g m_l}) + m_a(l_a + d_m s_p + l_h s_p) + m_b(l_{bx} s_p - l_{bx} c_p) + m_m(d_m + l_m)s_p}{m_a + m_b + m_l + m_m} \\ CoG_x^{ref} = 0 \end{cases} \quad (5.6)$$

## 5.2 Dynamics

The dynamic model of the TWFR requires the formulation of the relevant Euler-Lagrange equations. In this work, the formulation is done analyzing the potential energy and total kinetic energy of each body individually, it is important to mention that the wheels axis height is the reference height for the potential energy calculations. The notation  $I_\circ$  represents the inertia of the analyzed body  $\circ$  around the Y axis.

### 5.2.1 Wheels

For each robot's wheel, the kinetic and potential energy are defined by equations (5.7) and (5.8) respectively.

$$K_w(t) = \frac{1}{2} I_w \dot{\theta}_w^2 + \frac{1}{2} m_w r_w^2 \dot{\theta}_w^2 \quad (5.7)$$

$$U_w = 0 \quad (5.8)$$

### 5.2.2 Main body

The main body's kinetic and potential energy are defined by equations (5.9) and (5.10) respectively. The main body is composed of the original robot's body and the static part of the acquired actuator.

$$\begin{aligned} K_b(t) &= \frac{1}{2} m_b l_{bx}^2 \dot{\theta}_p^2 + \frac{1}{2} m_b l_{bz}^2 \dot{\theta}_p^2 + \frac{1}{2} m_b r_w^2 \dot{\theta}_w^2 \\ &\quad + \frac{1}{2} I_b \dot{\theta}_p^2 \\ &\quad + m_b \sin(\theta_p) l_{bx} r_w \dot{\theta}_w \dot{\theta}_p \\ &\quad + m_b \cos(\theta_p) l_{bz} r_w \dot{\theta}_w \dot{\theta}_p \end{aligned} \quad (5.9)$$

$$U_b(t) = g m_b (l_{bz} \cos(\theta_p) + l_{bx} \sin(\theta_p)) \quad (5.10)$$

### 5.2.3 Lift

Lift's kinetic and potential energy are defined by equations (5.11) and (5.12) respectively. The lift body is composed by the fork subassembly, its base plate and the mobile carriage of the linear actuator.

$$\begin{aligned}
K_m(t) = & \frac{1}{2} I_m \dot{\theta}_p^2 \\
& + m_m (\cos(\theta_p) \dot{d}_m - \sin(\theta_p) (l_m + d_m) \dot{\theta}_p) \\
& \times \left( \frac{1}{2} \cos(\theta_p) \dot{d}_m - \frac{1}{2} \sin(\theta_p) (l_m + d_m) \dot{\theta}_p \right) \\
& + m_m (\sin(\theta_p) \dot{d}_m + r_w \dot{\theta}_w + \cos(\theta_p) (l_m + d_m) \dot{\theta}_p) \\
& \times \left( \frac{1}{2} \sin(\theta_p) \dot{d}_m + \frac{1}{2} r_w \dot{\theta}_w + \frac{1}{2} \cos(\theta_p) (l_m + d_m) \dot{\theta}_p \right)
\end{aligned} \tag{5.11}$$

$$U_m(t) = g m_m \cos(\theta_p) (l_m + d_m) \tag{5.12}$$

### 5.2.4 Fork

Finally, the fork's kinetic and potential energy are defined by equations (5.13) and (5.14) respectively.

$$\begin{aligned}
K_a(t) = & I_a \left( \frac{\dot{\theta}_a}{2} + \frac{\dot{\theta}_p}{2} \right) (\dot{\theta}_a + \dot{\theta}_p) \\
& + m_a \left( -\cos(\theta_p) \dot{d}_m + l_a \cos(\theta_a + \theta_p) (\dot{\theta}_a + \dot{\theta}_p) \right. \\
& \quad \left. + \sin(\theta_p) d_m \dot{\theta}_p + l_h \sin(\theta_p) \dot{\theta}_p \right) \\
& \times \left( -\frac{1}{2} \cos(\theta_p) \dot{d}_m + \frac{1}{2} l_a \cos(\theta_a + \theta_p) (\dot{\theta}_a + \dot{\theta}_p) \right. \\
& \quad \left. + \frac{1}{2} \sin(\theta_p) d_m \dot{\theta}_p + \frac{1}{2} l_h \sin(\theta_p) \dot{\theta}_p \right) \\
& + m_a \left( \sin(\theta_p) \dot{d}_m + r_w \dot{\theta}_w + \cos(\theta_p) d_m \dot{\theta}_p \right. \\
& \quad \left. - l_a \sin(\theta_a + \theta_p) (\dot{\theta}_a + \dot{\theta}_p) + l_h \cos(\theta_p) \dot{\theta}_p \right) \\
& \times \left( \frac{1}{2} \sin(\theta_p) \dot{d}_m + \frac{1}{2} r_w \dot{\theta}_w + \frac{1}{2} \cos(\theta_p) d_m \dot{\theta}_p \right. \\
& \quad \left. - \frac{1}{2} l_a \sin(\theta_a + \theta_p) (\dot{\theta}_a + \dot{\theta}_p) + \frac{1}{2} l_h \cos(\theta_p) \dot{\theta}_p \right)
\end{aligned} \tag{5.13}$$

$$U_a(t) = g m_a (l_h \cos(\theta_p) - l_a \sin(\theta_a + \theta_p) + \cos(\theta_p) d_m) \tag{5.14}$$

### 5.2.5 Euler-Lagrange equation

With the presented individual kinetic and potential energies, the total kinetic and potential energy of the TWFR and the Lagrangian of the system are defined as follows.

$$K_{total} = K_w + K_b + K_m + K_a, \quad U_{total} = U_w + U_b + U_m + U_a \quad (5.15)$$

$$L = K_{total} - U_{total} \quad (5.16)$$

Finally, the Euler-Lagrange equation for the system is defined as,

$$\frac{d}{dt} \left( \frac{\partial L}{\partial \dot{q}} \right) - \frac{\partial L}{\partial q} = \tau \quad (5.17)$$

where

$$q = [\theta_w \quad \theta_p \quad d_m \quad \theta_a]^T \quad \text{and} \quad \tau = [n_w \tau_w \quad -n_w \tau_w \quad f_m \quad n_a \tau_a]^T \quad (5.18)$$

Equation (5.19) represents the solution of the presented Euler-Lagrange equation.

$$M = \begin{bmatrix} m_{11} & m_{12} & m_{13} & m_{14} \\ m_{21} & m_{22} & m_{23} & m_{24} \\ m_{31} & m_{32} & m_{33} & m_{34} \\ m_{41} & m_{42} & m_{43} & m_{44} \end{bmatrix} \quad (5.19)$$

$$H = \begin{pmatrix} h_1 \\ h_2 \\ h_3 \\ h_4 \end{pmatrix} \quad G = \begin{pmatrix} 0 \\ g_2 \\ g_3 \\ g_4 \end{pmatrix}$$

With,

$$\begin{aligned} m_{11} &= 2r_w^2 m_w + r_w^2 m_b + r_w^2 m_m + r_w^2 m_a + 2I_w \\ m_{12} &= (l_{bz} r_w \cos(\theta_p) + l_{bx} r_w \sin(\theta_p)) m_b \\ &\quad + (l_m r_w \cos(\theta_p) + r_w \cos(\theta_p) d_m) m_m \\ &\quad + (l_h r_w \cos(\theta_p) - l_a r_w \sin(\theta_a + \theta_p) + r_w \cos(\theta_p) d_m) m_a \\ m_{13} &= r_w \sin(\theta_p) (m_m + m_a) \\ m_{14} &= -l_a r_w \sin(\theta_a + \theta_p) m_a \\ m_{21} &= m_{12} \\ m_{22} &= (l_{bx}^2 + l_{bz}^2) m_b \\ &\quad + (l_m^2 + 2l_m d_m + d_m^2) m_m \\ &\quad + (l_a^2 - 2 \sin(\theta_a) l_a l_h - 2 \sin(\theta_a) l_a d_m + l_h^2 + 2l_h d_m + d_m^2) m_a \\ &\quad + I_b + I_m + I_a \end{aligned}$$

$$m_{23} = -l_a \cos(\theta_a) m_a$$

$$m_{24} = (l_a^2 - l_a l_h \sin(\theta_a) - l_a \sin(\theta_a) d_m) m_a + I_a$$

$$m_{31} = m_{13}$$

$$m_{32} = m_{23}$$

$$m_{33} = m_m + m_a$$

$$m_{34} = -l_a \cos(\theta_a) m_a$$

$$m_{41} = m_{14}$$

$$m_{42} = m_{24}$$

$$m_{43} = m_{34}$$

$$m_{44} = l_a^2 m_a + I_a$$

$$h_1 = l_{bx} m_b r_w \cos(\theta_p(t)) (\dot{\theta}_p(t))^2 - l_{bz} m_b r_w \sin(\theta_p(t)) (\dot{\theta}_p(t))^2$$

$$- l_h m_a r_w \sin(\theta_p(t)) (\dot{\theta}_p(t))^2 - l_m m_m r_w \sin(\theta_p(t)) (\dot{\theta}_p(t))^2$$

$$- l_a m_a r_w \cos(\theta_a(t) + \theta_p(t)) (\dot{\theta}_a(t))^2 - l_a m_a r_w \cos(\theta_a(t) + \theta_p(t)) (\dot{\theta}_p(t))^2$$

$$- m_a r_w \sin(\theta_p(t)) d_m(t) (\dot{\theta}_p(t))^2 - m_m r_w \sin(\theta_p(t)) d_m(t) (\dot{\theta}_p(t))^2$$

$$+ 2 m_a r_w \cos(\theta_p(t)) \dot{\theta}_p(t) \dot{d}_m(t) + 2 m_m r_w \cos(\theta_p(t)) \dot{\theta}_p(t) \dot{d}_m(t)$$

$$- 2 l_a m_a r_w \cos(\theta_a(t) + \theta_p(t)) \dot{\theta}_p(t) \dot{\theta}_a(t)$$

$$h_2 = 2 m_a d_m(t) \dot{\theta}_p(t) \dot{d}_m(t) + 2 m_m d_m(t) \dot{\theta}_p(t) \dot{d}_m(t) + 2 l_h m_a \dot{\theta}_p(t) \dot{d}_m(t)$$

$$+ 2 l_m m_m \dot{\theta}_p(t) \dot{d}_m(t) - 2 l_a m_a \sin(\theta_a(t)) \dot{\theta}_p(t) \dot{d}_m(t)$$

$$- l_a l_h m_a \cos(\theta_a(t)) (\dot{\theta}_a(t))^2 - l_a m_a \cos(\theta_a(t)) d_m(t) (\dot{\theta}_a(t))^2$$

$$- 2 l_a l_h m_a \cos(\theta_a(t)) \dot{\theta}_p(t) \dot{\theta}_a(t) - 2 l_a m_a \cos(\theta_a(t)) d_m(t) \dot{\theta}_p(t) \dot{\theta}_a(t)$$

$$h_3 = l_a m_a \sin(\theta_a(t)) (\dot{\theta}_a(t))^2 - l_m m_m (\dot{\theta}_p(t))^2 - m_a d_m(t) (\dot{\theta}_p(t))^2$$

$$- m_m d_m(t) (\dot{\theta}_p(t))^2 - l_h m_a (\dot{\theta}_p(t))^2 + l_a m_a \sin(\theta_a(t)) (\dot{\theta}_p(t))^2$$

$$+ 2 l_a m_a \sin(\theta_a(t)) \dot{\theta}_p(t) \dot{\theta}_a(t)$$

$$h_4 = l_a l_h m_a \cos(\theta_a(t)) (\dot{\theta}_p(t))^2 - 2 l_a m_a \sin(\theta_a(t)) \dot{\theta}_p(t) \dot{d}_m(t)$$

$$+ l_a m_a \cos(\theta_a(t)) d_m(t) (\dot{\theta}_p(t))^2$$

and

$$g_2 = g m_b (l_{bx} \cos(\theta_p) - l_{bz} \sin(\theta_p))$$

$$- g m_a (l_h \sin(\theta_p) + l_a \cos(\theta_a + \theta_p))$$

$$- g \sin(\theta_p) d_m (m_a + m_m)$$

$$- g l_m m_m \sin(\theta_p)$$

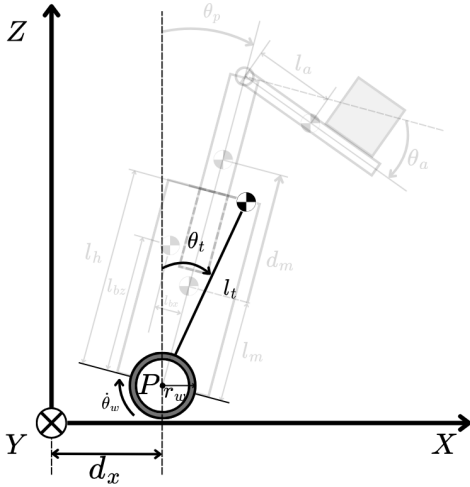


**Figure 5.2.1.** Simplified model of the TWFR.

$$g_3 = g \cos(\theta_p)(m_a + m_m)$$

$$g_4 = -g l_a m_a \cos(\theta_a + \theta_p)$$

## 5.2.6 Simplified dynamics

The above-presented expression is used in the following section to formulate the different control strategies. Nevertheless, an alternative representation of the system is used to define trajectory profiles for the robot. Figure 5.2.1 illustrates a simplified model of the TWFR where the robot is modeled as a single-link inverted pendulum with mass, length, and equivalent total pitch angle expressed by equations (5.20), (5.21), and (5.22), respectively.

$$m_t = m_b + m_m + m_a + m_l \quad (5.20)$$

$$l_t^2 = CoG_x^2 + CoG_z^2 \quad (5.21)$$

$$\theta_t = atan\left(\frac{CoG_x}{CoG_z}\right) \quad (5.22)$$

Once again, the kinetic and potential energy of the different bodies is calculated individually. In this simplified model, the above-presented equations for the wheels (5.7) and (5.8) will be used. However, the main body of the robot is simplified as a single-link ideal pendulum. Thus, equations (5.23) and (5.24) represent their kinetic and potential energy, respectively.

$$K(t) = m_t l_t^2 \dot{\theta}_t^2 + \frac{1}{2} m_t r_w^2 \dot{\theta}_w^2 + m_t \cos(\theta_t) l_t r_w \dot{\theta}_w \dot{\theta}_t \quad (5.23)$$

$$U(t) = g l_t m_t \cos(\theta_t) \quad (5.24)$$

Calculating the total kinetic and potential energy of the new simplified system, using equations (5.16), (5.17), and considering that,

$$q^* = [\theta_w \quad \theta_t]^T \quad \text{and} \quad \tau^*(\ddot{x}) = [n_w \tau_w(\ddot{x}) \quad -n_w \tau_w(\ddot{x})]^T \quad (5.25)$$

where,

$$\tau_w(\ddot{x}) = r_w m_t \dot{x}^{ref} \quad (5.26)$$

The solution of the Euler-Lagrange equation for the simplified system is presented in equation (5.27). With this simplified system, it is possible to establish a correlation between the angle  $\theta_t$  and the desired horizontal acceleration of the robot  $\ddot{x}$ .

$$\begin{aligned} M^*(q^*) \ddot{q}^* + H^*(\dot{q}^*, q^*) + G^*(q^*) &= \tau^*(\ddot{x}) \\ M^* &= \begin{pmatrix} m_{11}^* & m_{12}^* \\ m_{21}^* & m_{22}^* \end{pmatrix} \\ H^* &= \begin{pmatrix} h_1^* \\ 0 \end{pmatrix} \quad G^* = \begin{pmatrix} 0 \\ g_2^* \end{pmatrix} \end{aligned} \quad (5.27)$$

with

$$\begin{aligned} m_{11}^* &= 2r_w^2 m_w + r_w^2 m_t + 2I_w \\ m_{12}^* &= m_{21}^* = l_t r_w \cos(\theta_t) m_t \\ m_{22}^* &= 2l_t^2 m_t \\ h_1^* &= -l_t m_t r_w \sin(\theta_t) (\dot{\theta}_t)^2 \\ g_2^* &= -g l_t m_t \sin(\theta_t) \end{aligned}$$

With the presented formulation of the robot's kinematics and dynamics, the set of equations composed by equations (5.6), (5.21), and (5.27) is used along with small angle assumptions, to simplify trigonometric expressions, to find the reference values of  $\theta_p$ ,  $\dot{\theta}_p$ ,  $d_m$ , and  $\dot{d}_m$  that allow the robot to follow simultaneously the proposed motion profiles along the X axis for the entire robot and along the Z axis for the end effector. The solution was found numerically with MATLAB, which creates a solution block that will be used in the simulation environment.

# Chapter 6

## Control

The low-level control of the robot uses the complete dynamic formulation exposed in Chapter 5, more specifically, equation (5.19). The control architecture is composed of different disturbance observers and PD controllers for each subsystem as follows.

### 6.1 Synthesized Pitch Angle Disturbance Observer (SPADO)

SPADO is used to model the unified disturbances that affect the angle of the wheels and the pitch angle of the robot due to the underactuated condition of the system. Equations (6.1), (6.2), and (6.3) present the procedure to find the total disturbance over the wheel's angle caused by interference torques of the other subsystems, modeling errors, and external torques.

$$m_{11}\ddot{\theta}_w + m_{12}\ddot{\theta}_p + m_{13}\ddot{d}_m + m_{14}\ddot{\theta}_a + h_1 = n_w\tau_w - T_{lw} \quad (6.1)$$

$$m_{n11}\ddot{\theta}_w^{res} = n_w\tau_w^{ref} - \tilde{\tau}_w^{dist} \quad (6.2)$$

$$\begin{aligned} \tilde{\tau}_w^{dist} = & (m_{11} - m_{n11})\ddot{\theta}_w + m_{12}\ddot{\theta}_p \\ & + m_{13}\ddot{d}_m + m_{14}\ddot{\theta}_a + h_1 + T_{lw} \end{aligned} \quad (6.3)$$

Equations (6.4), (6.5), and (6.6) present the procedure to find the total disturbance over the pitch angle caused by interference torques of the other subsystems, modeling errors, and external torques.

$$\begin{aligned} m_{21}\ddot{\theta}_w + m_{22}\ddot{\theta}_p + m_{23}\ddot{d}_m + m_{24}\ddot{\theta}_a \\ + h_2 + g_2 = -n_w\tau_w - T_{lp} \end{aligned} \quad (6.4)$$

$$m_{n21}\ddot{\theta}_w^{res} + m_{n22}\ddot{\theta}_p^{res} = -n_w\tau_w^{ref} - \tilde{\tau}_p^{dist} \quad (6.5)$$

$$\begin{aligned} \tilde{\tau}_p^{dist} = & (m_{21} - m_{n21})\ddot{\theta}_w + (m_{22} - m_{n22})\ddot{\theta}_p \\ & + m_{23}\ddot{d}_m + m_{24}\ddot{\theta}_a + h_2 + g_2 + T_{lp} \end{aligned} \quad (6.6)$$

Equation (6.7) is obtained by substituting  $\ddot{\theta}_w$  from (6.2) in (6.5).

$$m_{n22}\ddot{\theta}_p^{res} + \frac{m_{n21} + m_{n11}}{m_{n11}}n_w\tau_w^{ref} = \frac{m_{n21}}{m_{n11}}\tilde{\tau}_w^{dis} - \tilde{\tau}_p^{dist} \quad (6.7)$$

Finally, the synthesized disturbance is expressed by equation (6.8)

$$\tilde{\tau}_s^{dist} = \tilde{\tau}_p^{dist} - \frac{m_{n21}}{m_{n11}}\tilde{\tau}_w^{dis} \quad (6.8)$$

Equation (6.9) expresses the synthesized disturbance as a function of the pitch angle acceleration and the torque of the wheels. By using pseudo-differentiation over  $\dot{\theta}_p^{res}$ , equation (6.10) estimates the total disturbance that will be added to the wheel's torque reference.

$$m_{n22}\ddot{\theta}_p^{res} + \frac{m_{n21} + m_{n11}}{m_{n11}}n_w\tau_w^{ref} = -\tilde{\tau}_s^{dist} \quad (6.9)$$

$$\begin{aligned} \hat{\tau}_s^{dist} &= \frac{g_s}{s + g_s} \left( g_s m_{n22} \dot{\theta}_p^{res} - \frac{m_{n21} + m_{n11}}{m_{n11}} n_w \tau_w^{ref} \right) \\ &\quad - g_s m_{n22} \dot{\theta}_p^{res} \end{aligned} \quad (6.10)$$

Figure 6.1.1 shows the block diagram that represents the implementation of the SPADO observer in the control architecture.

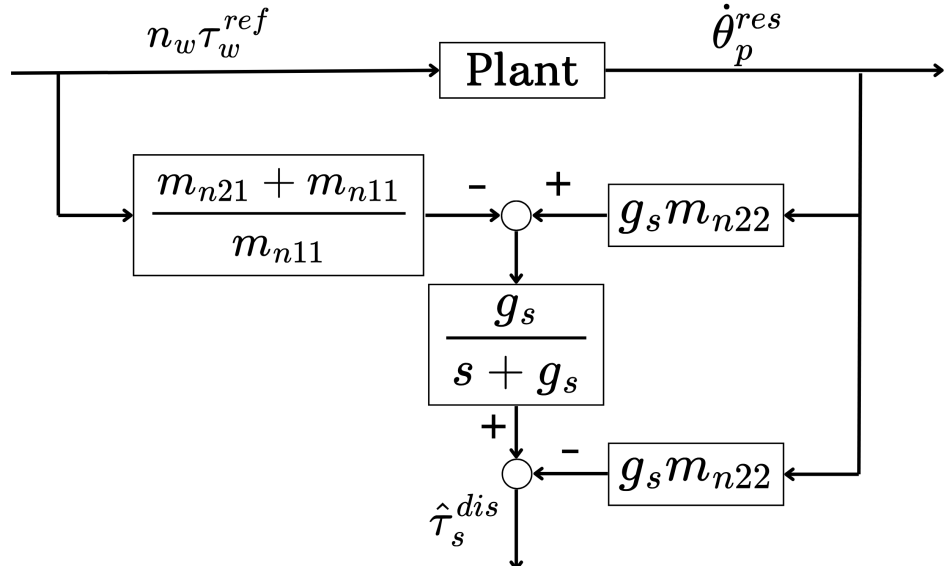


**Figure 6.1.1.** Block diagram SPADO.

## 6.2 Pitch Angle Control

The vertical stabilization of the robot is accomplished by a PD controller implemented for the robot's pitch angle. The reference torque is determined using the candidate Lyapunov function (6.11) to guarantee a convergent behavior for the pitch angle. With equations (6.12) and (6.13), it is possible to find an expression for  $\ddot{\theta}_p^{res}$  that is used in equation (6.9) to determine the reference torque for the wheels to keep the robot's body vertically. This reference torque is expressed in equation (6.14).

$$V = \frac{1}{2}K_1(\dot{\theta}_p^{cmd} - \dot{\theta}_p^{res})^2 + \frac{1}{2}K_2(\ddot{\theta}_p^{cmd} - \ddot{\theta}_p^{res})^2 \quad (6.11)$$

$$\dot{V} = (\dot{\theta}_p^{cmd} - \dot{\theta}_p^{res})(K_1(\dot{\theta}_p^{cmd} - \dot{\theta}_p^{res}) + K_2(\ddot{\theta}_p^{cmd} - \ddot{\theta}_p^{res})) \quad (6.12)$$

$$\dot{V} = -K_3(\dot{\theta}_p^{cmd} - \dot{\theta}_p^{res})^2 \quad (6.13)$$

$$\begin{aligned} \tau_w^{ref} = & -\frac{m_{n11}m_{n22}}{n_w(m_{n21} + m_{n11})}(K_{pp}(\dot{\theta}_p^{cmd} - \dot{\theta}_p^{res}) \\ & + K_{dp}(\dot{\theta}_p^{cmd} - \dot{\theta}_p^{res}) + \ddot{\theta}_p^{cmd}) \\ & - \frac{m_{n11}}{n_w(m_{n21} + m_{n11})}\hat{\tau}_s^{dist} \end{aligned} \quad (6.14)$$

$$K_{pp} = \frac{K_1}{K_2}, \quad K_{dp} = \frac{K_3}{K_2} \quad (6.15)$$

Analyzing the expression (6.14), it is possible to see that it depends on the synthesized disturbance. Thus, the complete SPADO-PD controller architecture is depicted in Figure 6.2.1.

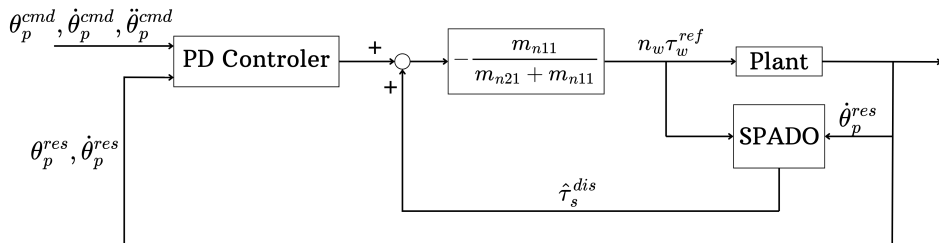


**Figure 6.2.1.** Block diagram SPADO-PD controller pitch angle.

## 6.3 Fork Disturbance Observer (FDOB)

Similarly, as it was previously presented, equations (6.16), (6.17), and (6.18) present the procedure to find the total disturbance over the fork angle caused by interference torques of the other subsystems, modeling errors, and external torques.

$$m_{41}\ddot{\theta}_w + m_{42}\ddot{\theta}_p + m_{43}\ddot{\theta}_m + m_{44}\ddot{\theta}_a + h_4 + g_4 = n_a\tau_a - T_{la} \quad (6.16)$$

$$m_{n44}\ddot{\theta}_a^{res} = n_a\tau_a^{ref} - \tilde{\tau}_a^{dist} \quad (6.17)$$

$$\begin{aligned} \tilde{\tau}_a^{dist} &= m_{41}\ddot{\theta}_w^{res} + m_{42}\ddot{\theta}_p^{res} + m_{43}\ddot{\theta}_m^{res} \\ &\quad + (m_{44} - m_{n44})\ddot{\theta}_a^{res} + h_4 + g_4 + T_{la} \end{aligned} \quad (6.18)$$

FDOB uses the pseudo-differentiation method over  $\dot{\theta}_a^{res}$  to estimate the disturbance torque.

$$\hat{\tau}_a^{dist} = \frac{g_a}{s + g_a}(n_a\tau_a^{ref} + g_a m_{n44}\dot{\theta}_a^{res}) - g_a m_{n44}\dot{\theta}_a^{res} \quad (6.19)$$

Figure 6.3.1 shows the block diagram that represents the implementation of the FDOB observer in the control architecture.

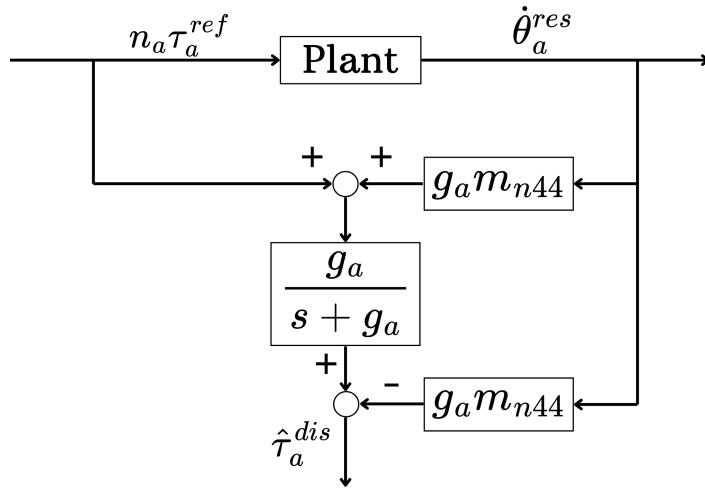


**Figure 6.3.1.** Block diagram FDOB.

## 6.4 Fork Angle Control

For the fork subsystem, a PD controller is implemented that also considers the estimated disturbance torque as it is presented in (6.20)

$$\tau_a^{ref} = K_{pa}(\theta_a^{cmd} - \theta_a^{res}) + K_{da}(\dot{\theta}_a^{cmd} - \dot{\theta}_a^{res}) + \hat{\tau}_a^{dist} \quad (6.20)$$

Thus, the complete FDOB-PD controller architecture is depicted in Figure 6.4.1.

## 6.5 Fork Reaction Torque Observer (FROB)

By modeling the external load-dependent torque as (6.21), evaluating it in (6.18), and reorganizing the terms by making the disturbance torque independent of the effects of gravity and friction (6.22), (6.23), the reaction torque of the fork due to an external load is obtained by (6.24).

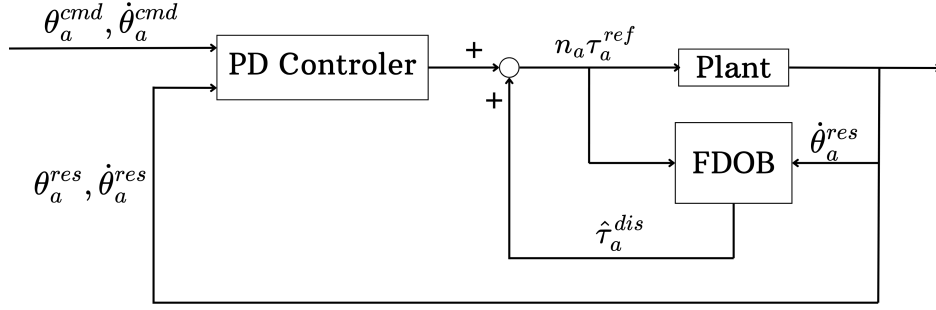


**Figure 6.4.1.** Block diagram FDOB-PD controller fork angle.

$$T_{la} = \tilde{\tau}_a^{ext} + \tilde{\tau}_a^{fric} \quad (6.21)$$

$$\begin{aligned} \tilde{\tau}_a^{reac} = & m_{41}\ddot{\theta}_w^{res} + m_{42}\ddot{\theta}_p^{res} + m_{43}\ddot{d}_m^{res} \\ & + (m_{44} - m_{n44})\ddot{\theta}_a^{res} + h_4 + \tilde{\tau}_a^{ext} \end{aligned} \quad (6.22)$$

$$m_{n44}\ddot{\theta}_a^{res} = n_a \tau_a^{ref} - g_4 - \tilde{\tau}_a^{fric} - \tilde{\tau}_a^{reac} \quad (6.23)$$

$$\begin{aligned} \hat{\tau}_a^{reac} = & \frac{g_r}{s + g_r} (n_a \tau_a^{ref} + g_r m_{n44} \dot{\theta}_a^{res} \\ & - g_4 - \tilde{\tau}_a^{fric}) - g_r m_{n44} \dot{\theta}_a^{res} \end{aligned} \quad (6.24)$$

Figure 6.5.1 shows the block diagram that represents the implementation of the FROB observer in the control architecture.

This reaction torque is related to the term  $t_l$  used in the kinematics equations as follows  
 $t_l = -\hat{\tau}_a^{reac}$

## 6.6 Lift Disturbance Observer (LDOB)

Analogously, as it was made for the fork subsystem, equations (6.25), (6.26), and (6.27) present the procedure to find the total disturbance over the lift displacement caused by interference forces of the other subsystems, modeling errors, and external forces.

$$m_{31}\ddot{\theta}_w + m_{32}\ddot{\theta}_p + m_{33}\ddot{d}_m + m_{34}\ddot{\theta}_a + h_3 + g_3 = f_m - F_{lm} \quad (6.25)$$

$$m_{n33}\ddot{d}_m^{res} = f_m^{ref} - \tilde{f}_m^{dist} \quad (6.26)$$

$$\tilde{f}_m^{dist} = m_{31}\ddot{\theta}_w^{res} + m_{32}\ddot{\theta}_p^{res} + (m_{33} - m_{n33})\ddot{d}_m^{res}$$

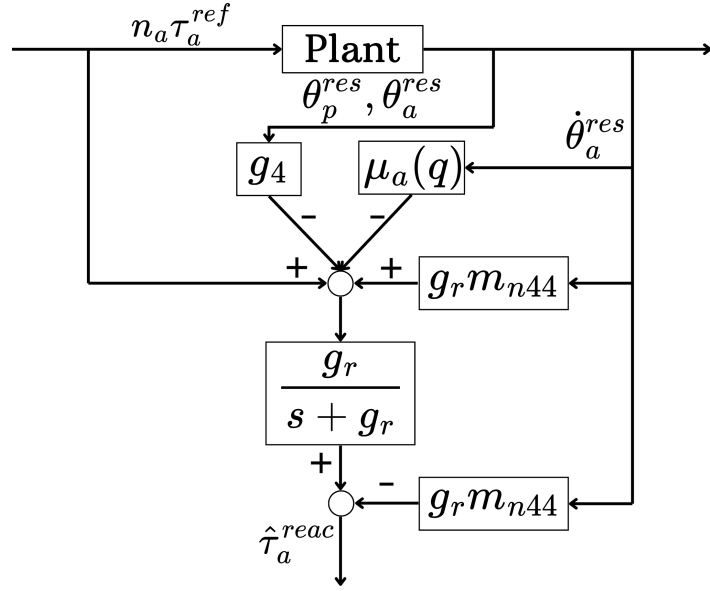


**Figure 6.5.1.** Block diagram FRTOB.

$$+ m_{34} \ddot{\theta}_a^{res} + h_3 + g_3 + F_{lm} \quad (6.27)$$

LDOB uses the pseudo-differentiation method over  $\dot{d}_m^{res}$  to estimate the disturbance force.

$$\hat{f}_m^{dist} = \frac{g_m}{s + g_m} (f_m^{ref} + g_m m_{n33} \dot{d}_m^{res}) - g_m m_{n33} \dot{d}_m^{res} \quad (6.28)$$

Figure 6.6.1 shows the block diagram that represents the implementation of the FDOB observer in the control architecture.

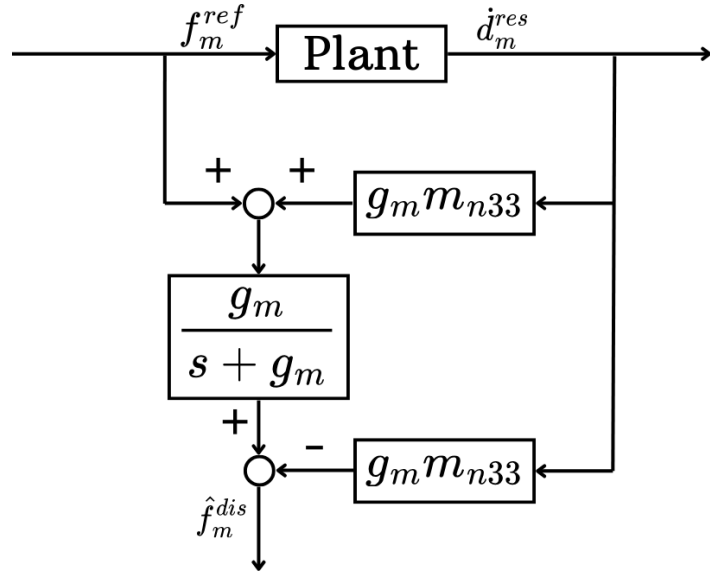


**Figure 6.6.1.** Block diagram LDOB.

## 6.7 Lift Displacement Control

Again, a PD controller is implemented that also considers the estimated disturbance force as it is presented in (6.29). Thus, the complete LDOB-PD controller architecture is depicted in Figure 6.7.1.

$$f_m^{ref} = K_{pm}(d_m^{cmd} - d_m^{res}) + K_{dm}(\dot{d}_m^{cmd} - \dot{d}_m^{res}) + \hat{f}_m^{dist} \quad (6.29)$$

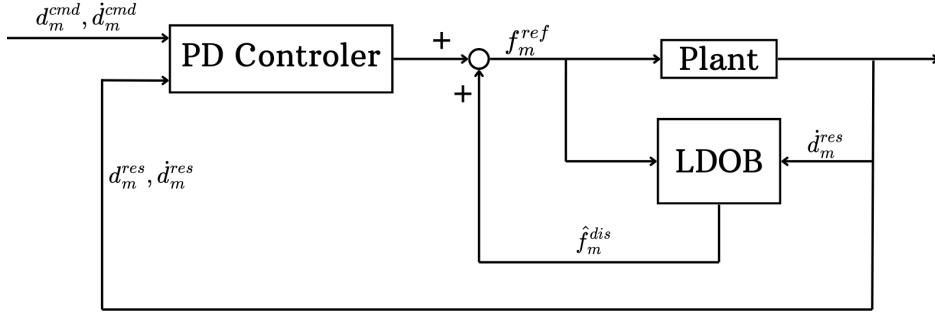


**Figure 6.7.1.** Block diagram LDOB-PD controller lift displacement.

## 6.8 Lift Reaction Force Observer (LRFOB)

By modeling the external load-dependent force as (6.30), evaluating it in (6.27), and reorganizing the terms by making the disturbance force independent of the effects of gravity and friction, the reaction force of the fork due to an external load is obtained by (6.31).

$$F_{lm} = \tilde{f}_m^{ext} + \tilde{f}_m^{fric} \quad (6.30)$$

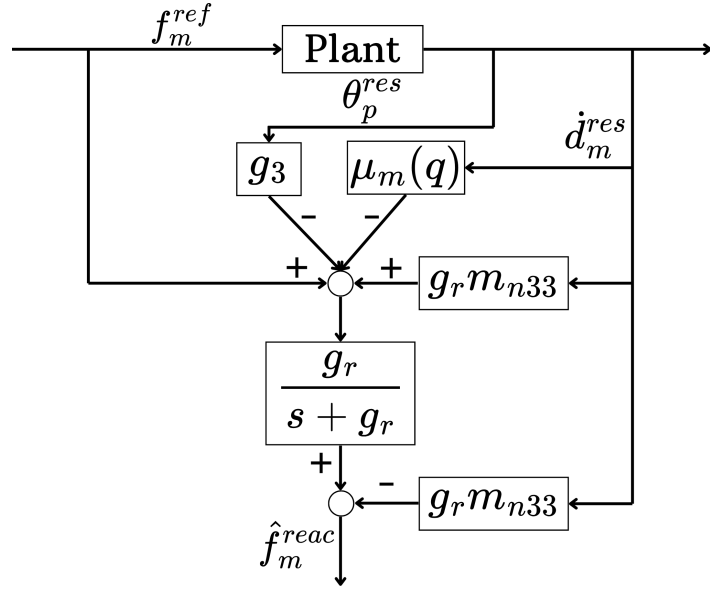
$$\begin{aligned} \hat{f}_m^{reac} &= \frac{g_r}{s+g_r} (f_m^{ref} + g_r m_{n33} \dot{d}_m^{res} \\ &\quad - g_3 - \tilde{f}_m^{fric}) - g_r m_{n33} \dot{d}_m^{res} \end{aligned} \quad (6.31)$$

Figure 6.8.1 shows the block diagram that represents the implementation of the LRFOB observer in the control architecture.

This reaction force is related to the term  $m_l$  used in the kinematics equations as follows  
 $m_l = \frac{\hat{f}_m^{reac}}{g \cos(\theta_p)}$

## 6.9 Wheel Position Control

Finally, the position control of the wheels is determined by setting a reference command for the pitch angle of the robot; this reference command is determined by the following



**Figure 6.8.1.** Block diagram LRFOB.

PD controller.

$$\theta_p^{cmd-PD} = K_{pw}(\theta_w^{cmd} - \theta_w^{res}) + K_{dw}(\dot{\theta}_w^{cmd} - \dot{\theta}_w^{res}) \quad (6.32)$$

Thus, the total pitch angle reference command is determined by the inverse solution and the PD controller.

$$\theta_p^{cmd} = \theta_p^{cmd-IS} + \theta_p^{cmd-PD} \quad (6.33)$$

## 6.10 Control architecture

The complete control architecture of the TWFR, including all the above-proposed observers, controllers, and reference generators, is presented in Figure 6.10.1.

## 6.11 Physical implementation

The above-presented control architecture was implemented in MATLAB-Simulink. Nevertheless, for the physical implementation, it is important to define the characteristics of the plant, including the communication protocols. For the real TWFR, the control algorithm code is implemented in a desk computer that runs the software MATLAB. This computer communicates with a Beckhoff Industrial PC through LAN communication, which is in charge of gathering all the feedback information from the motors and sensors and also sends the appropriate commands to them. The Industrial PC communicates with the servo-drivers and sensors using the EtherCAT protocol, as it is shown in Figure 6.11.1.

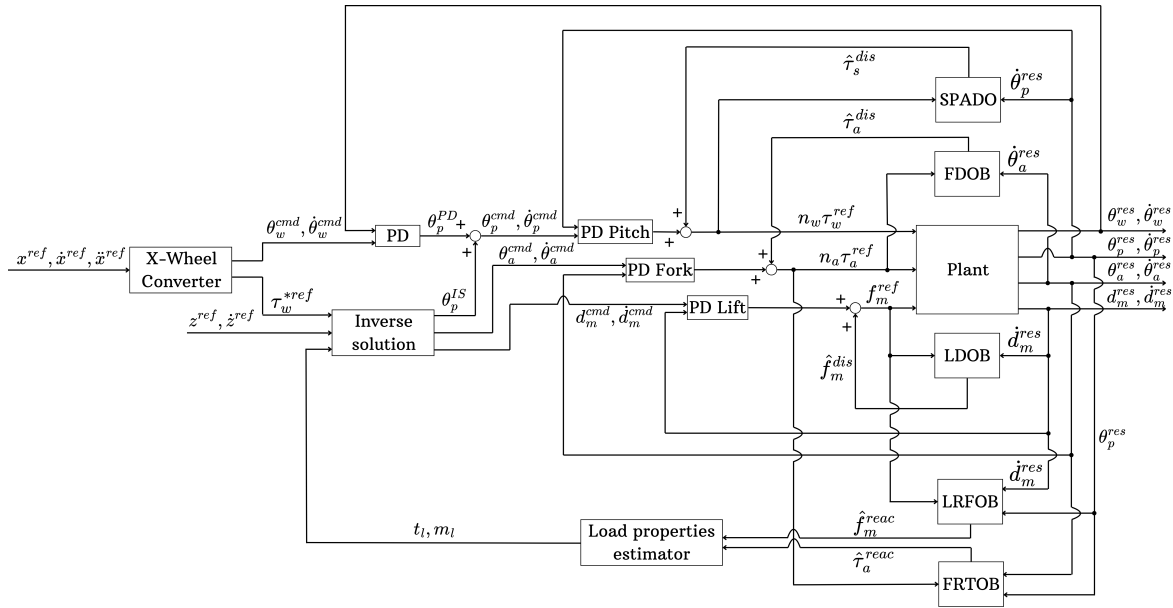


**Figure 6.10.1.** Block diagram of the complete control architecture of the TWFR.

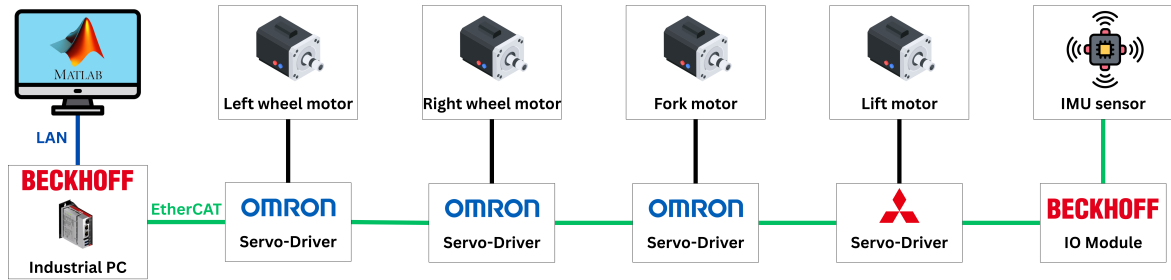


**Figure 6.11.1.** Hardware control architecture.

As can be seen, in the TWFR system, elements from different manufacturers interact with each other thanks to the EtherCAT protocol. This feature shows how convenient it is to have a unified industrial communication protocol for the hardware architecture, making the system modular and easily scalable. It is important to mention that the acquired linear actuator came with a servo-driver that communicates only with the Modbus RTU protocol. This device could only communicate with the control network using an EtherCat-Modbus gateway; however, this solution was inconvenient due to the current configuration of the robot. That is why it was required to order an EtherCAT-compatible Mitsubishi servo-driver, simplifying the installation and future scalability of the system. Nevertheless, this driver did not arrive in time to test the proposed control architecture physically in the system, as it was previously mentioned.

# Chapter 7

## Simulation results

### 7.1 Simulation parameters

Table 7.1.1 presents the simulation parameters used to characterize the controllers, observers, and physical properties of the TWFR.

**Table 7.1.1.** Experimental parameters

Parameter	Explanation	Value
$K_{pp}$	P-gain of pitch angle control	200
$K_{pd}$	D-gain of pitch angle control	50
$K_{pa}$	P-gain of arm position control	200
$K_{da}$	D-gain of arm position control	50
$K_{pm}$	P-gain of lift position control	200
$K_{dm}$	D-gain of lift position control	50
$K_{pw}$	P-gain of wheel position control	0.07
$K_{dw}$	D-gain of wheel position control	0.09
$g_s$ (rad/s)	Cutoff angular frequency of SPADO	$2\pi 6$
$g_a$ (rad/s)	Cutoff angular frequency of arm FDOB	$2\pi 5$
$g_r$ (rad/s)	Cutoff angular frequency of FRTOB, LRFOB	$2\pi 1$
$g_m$ (rad/s)	Cutoff angular frequency of LDOB	$2\pi 4$
$N_w$	Wheel gear ratio	11
$N_a$	Arm gear ratio	33
$I_{wy}$ ( $\text{kg m}^2$ )	Wheel inertia	0.0052
$I_{by}$ ( $\text{kg m}^2$ )	Body inertia	4.0590
$I_{my}$ ( $\text{kg m}^2$ )	Lift inertia	0.0482
$I_{ay}$ ( $\text{kg m}^2$ )	Arm inertia	0.0890
$l_{bz}$ (m)	Body CoG z coordinate	0.3206
$l_{bx}$ (m)	Body CoG x coordinate	0.0246
$l_m$ (m)	Lift CoG distance	0.3975
$l_a$ (m)	Arm CoG distance	0.2200
$m_w$ (kg)	Wheel mass	1.21
$m_b$ (kg)	Body mass	64.1
$m_m$ (kg)	Lift mass	21.5
$m_a$ (kg)	Arm mass	3.5
$m_l$ (kg)	Load mass	5

## 7.2 Proposed task

The simulation scenario was implemented in MATLAB-Simulink using the SimScape library, which is meant for modeling the dynamic behavior of mechanical systems with a powerful physics motor that simulates interactions between rigid bodies and environmental forces. Figure 7.2.1 illustrates a simplified model of the TWFR in the proposed simulation environment with an external load placed over the robot's fork. This proposed model simplifies the geometry of the TWFR to regular polyhedra to speed up the performance of the simulation while keeping the results as close as possible to the real behavior.

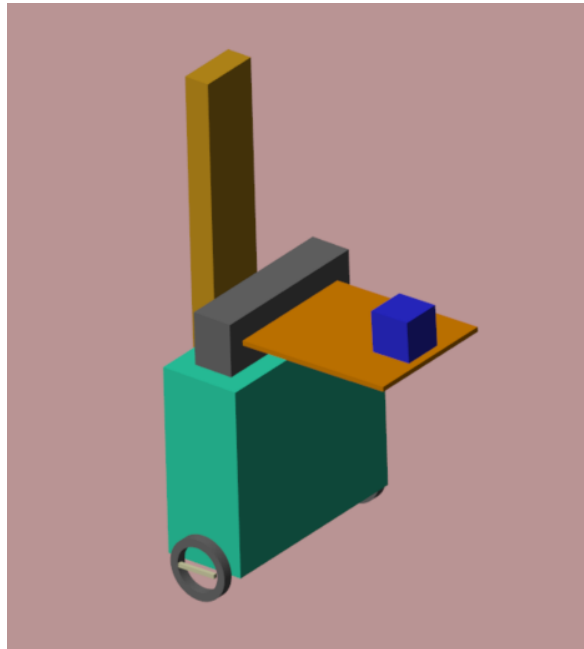


**Figure 7.2.1.** Model of TWFR in the simulation environment of MATLAB-Simulink.

A simple sequence of actions was designed to evaluate the performance of the proposed control and trajectory generation method in simulation. In the proposed scenario, the robot is carrying a load of 5kg placed over the fork at 0.37m from its rotational axis. The sequence begins with preliminary position stabilization, which is necessary after the initial perturbation caused by the placement of the external load. When the desired initial position is reached, the fork will lift the load from the initial Z coordinate of 0.6025 m to the final height set at 0.9 m. Afterwards, the robot will move forward 3m following the designed trajectory. During the execution of this horizontal movement, the fork will lower itself to its initial height and then rise again to 0.9m. When the robot reaches the desired position, the fork will lower the load to 0.7m, and simultaneously, it will move backward to the initial x-coordinate, following the same trajectory profile previously used.

### 7.3 Reference motion profiles

As explained in Chapter 6, the system's inputs are the reference motion profiles along the X and Z axes. In particular, it is important to define the desired position and acceleration profiles along the X axis and the position and velocity profiles along the Z axis. Figures 7.3.1 and 7.3.2 show the proposed motion profiles using the motion parameters defined in Table 7.3.1. Trapezoidal motion profiles were designed for the acceleration on the X axis and the velocity on the Z axis, according to the mechanical restrictions of the system. Considering that the horizontal motion is directly linked with the robot's pitch angle, its motion must be carefully designed; thus, a trapezoidal acceleration profile provides limits in the jerk of the motion, generating smooth trajectories. These motion profiles will be used as inputs to the trajectory generator proposed in Chapter 5 as the inverse solution block.

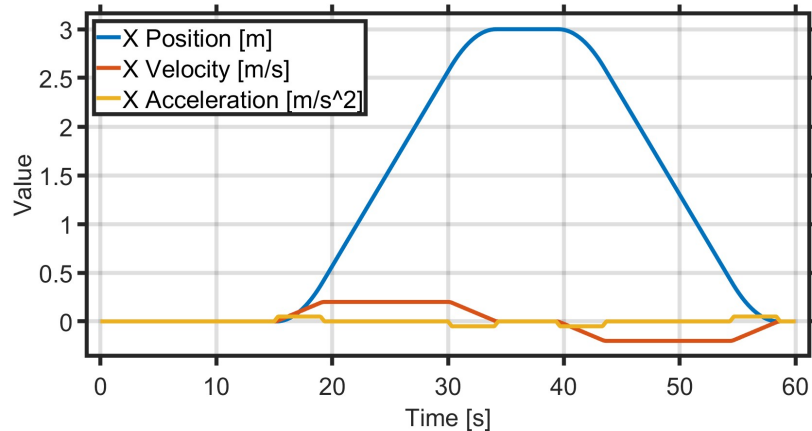


**Figure 7.3.1.** Reference position, velocity, and acceleration profiles of the TWFR along the X coordinate.

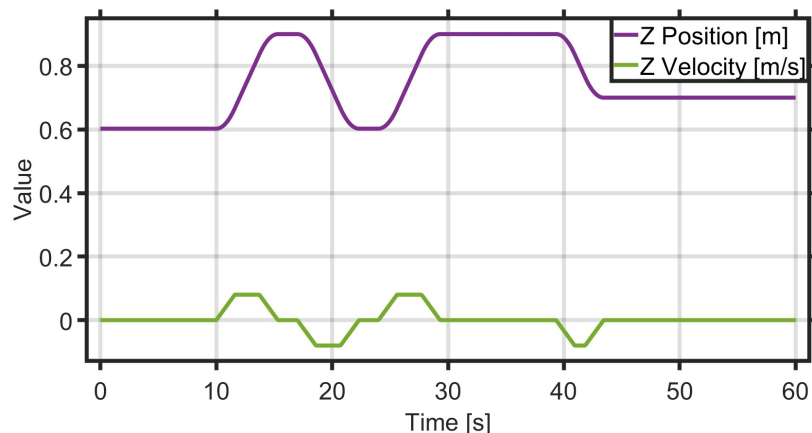


**Figure 7.3.2.** Reference position and velocity of the TWFR's fork along the Z coordinate.

**Table 7.3.1.** Motion profiles parameters

Parameter	Explanation	Value
$\dot{x}_{max}$ (m/s)	Maximum horizontal velocity	0.2
$\ddot{x}_{max}$ (m/s <sup>2</sup> )	Maximum horizontal acceleration	0.05
$\dddot{x}_{max}$ (m/s <sup>3</sup> )	Maximum horizontal jerk	0.15
$\dot{z}_{max}$ (m/s)	Maximum vertical velocity	0.08
$\ddot{z}_{max}$ (m/s <sup>2</sup> )	Maximum vertical acceleration	0.05

## 7.4 Response along X-axis

Position reference, system's response along the X axis, and the position error are shown in Figure 7.4.1 and Figure 7.4.2. These graphs demonstrate how the robot is capable of following the proposed position profile with a maximum transient state error of 14.7cm, which occurred because of the initial perturbation caused by the external load. On the other hand, the steady state position error reaches a maximum value of 1.7cm during the execution of the proposed trajectory.

Furthermore, as can be seen, the profile shapes for  $x$  and  $\ddot{x}$  were designed to limit the maximum jerk for the horizontal motion and thus, the jerk of the wheel's motors. Limiting this jerk avoids velocity overshoots that could cause the robot to go out of the stability region and also allows the system to have a smooth locomotion behavior during the execution of different motion tasks.

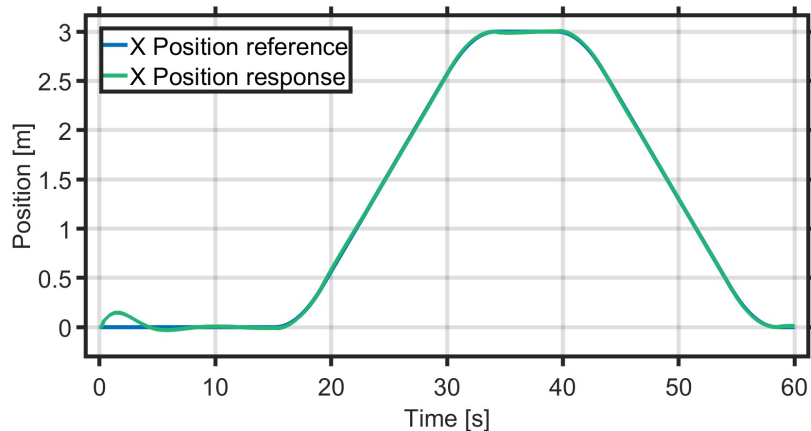


**Figure 7.4.1.** Reference and response position of the TWFR along the X coordinate.

The designed S-velocity profile for  $\dot{x}$  avoids possible oscillations during the execution of the movement. This characteristic is appreciated in Figure 7.4.3, which exhibits the response of the horizontal velocity of the system in contrast to the proposed reference. The velocity response of the TWFR presents overshoots at the corners of the profile, which correspond with changes in the acceleration profile.

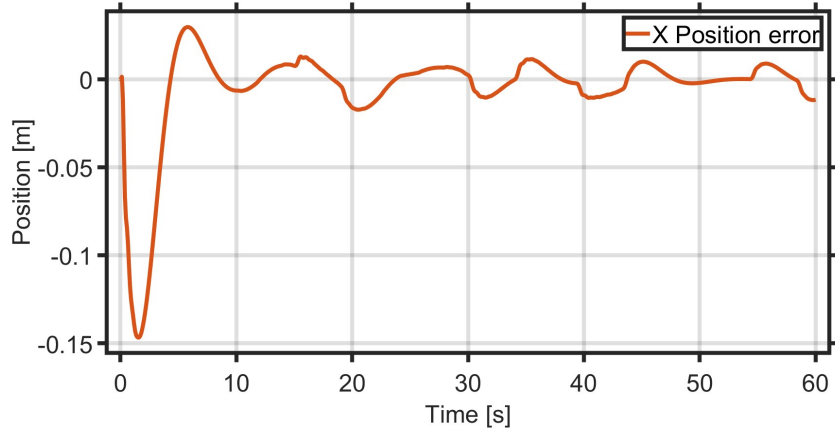


**Figure 7.4.2.** Position error of the TWFR along the X coordinate during the execution of the proposed task.

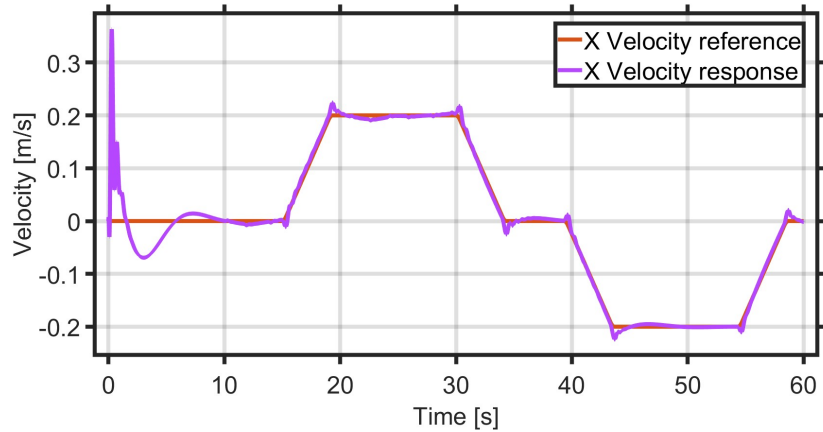


**Figure 7.4.3.** Reference S-shape profile and response velocity of the TWFR along the X coordinate.

## 7.5 Response along Z-axis

On the other hand, position reference, system's response along the Z axis, is shown in Figure 7.5.1. nevertheless, because of the high accuracy response obtained with the proposed method, Figure 7.5.2 illustrates the Z position error to get a better understanding of the motion performance. The Z position of the fork follows the proposed trajectory with a maximum error of 7.58mm during the transient state and 0.3mm in the steady state.

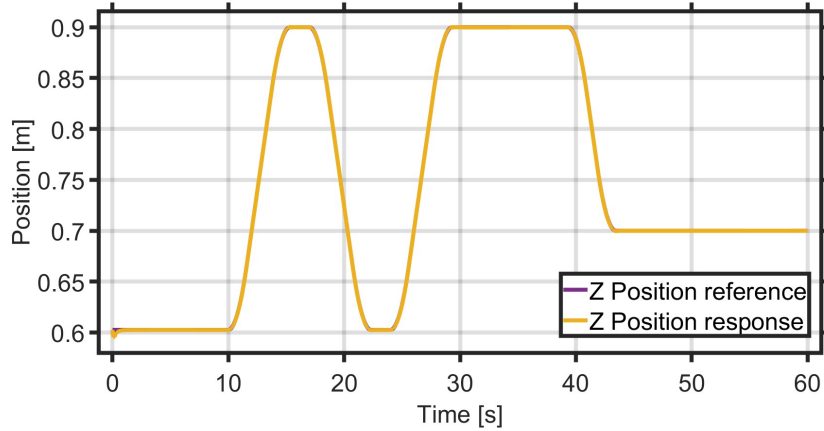


**Figure 7.5.1.** Reference and response position of the fork along the Z coordinate.

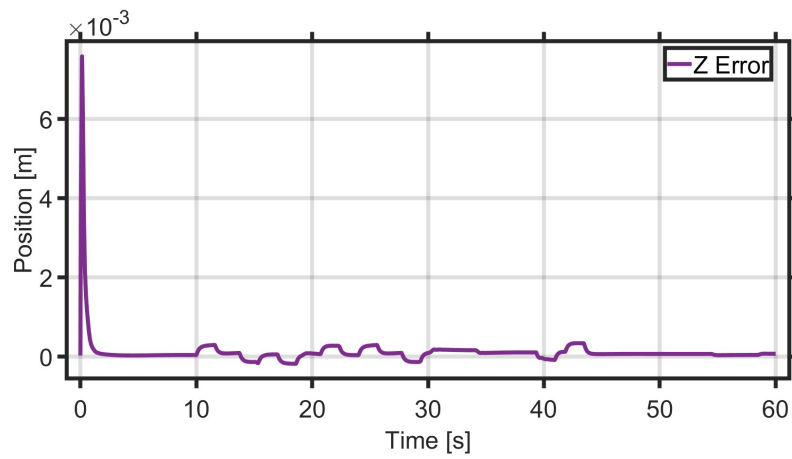


**Figure 7.5.2.** Position error of the fork along the Z coordinate during the execution of the proposed task.

## 7.6 Parameter estimation of external load

Finally, the performance of the FRTOB and the LRFOB is evaluated in Figure 7.6.1 and Figure 7.6.2, respectively, estimating the value  $t_l$  and  $m_l$  that corresponds to the generated torque and the mass of the external load. It is possible to see how the dynamic behavior of both estimations is fast during the transient state and is almost a constant value during the steady state, which is beneficial for the IK and ID solutions that depend on these variables for the appropriate calculation of the motion profiles. This estimation method is valid in this ideal simulation scenario because it does not consider the friction characteristics of the used actuators. In the real implementation of the control architecture, the obtained results will significantly change, especially for the LRFOB because of the high rigidity of the mechanical components used in the ball-screw linear mechanism.

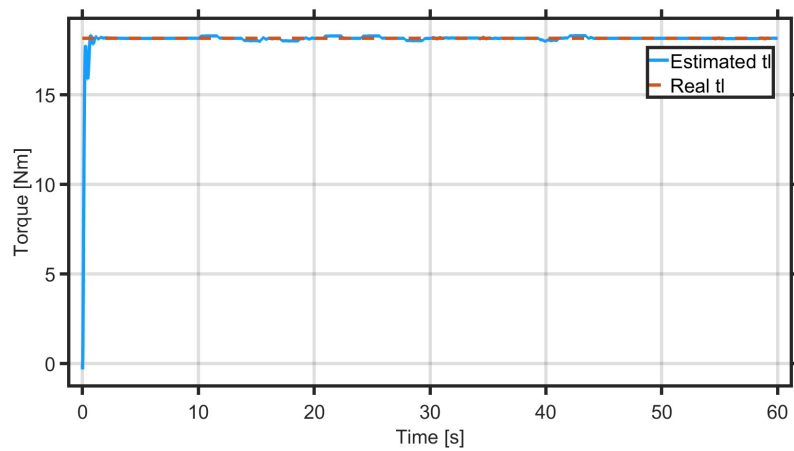


**Figure 7.6.1.** Estimated value of the torque caused by the external load of 5kg placed at 0.37m from the rotational axis of the fork (18.142Nm).

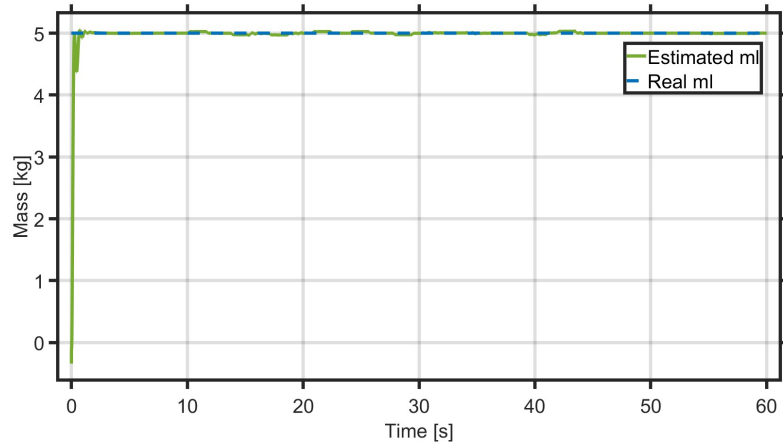


**Figure 7.6.2.** Estimated value of the mass of the external load (5kg).

# **Chapter 8**

## **Discussion**

### **8.1 Proposed task**

The designed specific sequence of movements aims to demonstrate the capabilities of the proposed methods by executing simultaneous motion along the X and Z axes, while dynamically tracking the changes in the external load to be manipulated. Following that idea, it is possible to classify the TWFR as a loco-manipulation system that allows the simultaneous execution of locomotion and manipulation tasks. In a complete manipulation task, the contact forces of the robot with the environment must be considered in the control design to avoid unpredictable behavior in the system's response. Nevertheless, this modeling is out of the scope of the current research. That is why it is assumed that the load is placed at the beginning of the simulation scenario.

### **8.2 Reference motion profiles**

The maximum velocity and acceleration limits were decided arbitrarily following an initial task intuition that considers the constraints of the aimed industrial setup. For the X-axis motion, the most restrictive variable is the acceleration profile, and consequently, the maximum jerk, because of the direct relation between the horizontal motion and the vertical stability of the robot. On the other hand, the acceleration in the Z-axis was designed to limit the interference torques that the lift subsystem has on the complete performance of the system. During the experiments, it was noticed that a high acceleration value in the vertical velocity generated oscillations on the horizontal velocity response of the TWFR.

### **8.3 Motion response**

The obtained error values demonstrate that the proposed control architecture and motion generator allow the robot to follow motion tasks within an acceptable precision for the

kind of environment where the robot is going to be deployed in a real-world scenario. These results must be further analyzed in the real robot to evaluate the robustness of the control architecture and its capability of rejecting external disturbances as friction, load variations, and unmodeled dynamics. However, with the obtained simulated results, it can be seen that the system properly tracked the proposed motion profiles in both coordinate axes, demonstrating the effectiveness of the proposed method.

## 8.4 Parameter estimation

These results are the most difficult to recreate in a real-world scenario due to their dependence on the mechanical properties of the hardware configuration of the robot. In particular, the lift subsystem mechanism imposes a significant limitation due to its stiffness and low friction, creating a mechanical barrier for the LRFOB to register the disturbance caused by the placement of the external load. On the other hand, the FRTOB has been tested in previous works, and the mechanical properties of the fork subsystem have proved to be ideal for the proper performance of the observer.

## 8.5 Physical implementation

As it has been mentioned in other chapters, the physical implementation of the presented methods was not completed on time because of problems with the acquisition of the driver of the lift subsystem's motor. All the necessary parts were manufactured and assembled in subsystems that can be easily added to the main structure of the current TWFR. Nevertheless, the obtained results prove the capabilities of the current work and offer a positive perspective to achieve interesting results for future implementations on the real system.

# Chapter 9

## Conclusions

As it was demonstrated throughout this work, the proposed motion planning and control strategies allow the TWFR to execute trajectories in the X and Z coordinate axes simultaneously with an admissible position error. However, it is important to mention that the dynamic characteristics of the robot impose limits on the possible motion profiles that can be generated, especially in the X axis. These limits must be evaluated experimentally to consider not only the theoretical constraints but also the effects of the disturbances generated by unmodeled dynamics and interactions with the environment.

The implementation of adaptive IK and ID solutions that depend on the estimation of physical properties of the external load provides great flexibility in industrial environments where it is not possible to control the variables of the load that will be manipulated. The estimation was achieved using disturbance observers that rely on mechanical properties of the used components as stiffness and friction. In a future physical implementation, the mechanical properties of the ball-screwed linear mechanism will limit the effectiveness of the observer because most of the external disturbance will be counteracted by the mechanical rigidity of the mechanism, restricting the movement of the lift and consequently the rotation of the motor's shaft.

The next steps for this work are the construction of the lift subsystem and the physical implementation of the presented motion planning and control algorithms. All the mechanical and motion generation components were acquired and are ready to be implemented in the current TWFR. The EtherCAT network must be expanded to include the driver of the lift subsystem, and thus, a different architecture has to be implemented in the original MATLAB controller. With the presented results, it is expected that the real system will show promising results with the proposed control and trajectory generation methods.

# Bibliography

- [1] P. K. W. Abeygunawardhana, M. Defoort, and T. Murakami, “Self-sustaining control of two-wheel mobile manipulator using sliding mode control”, *The 11th IEEE International Workshop on Advanced Motion Control*, Mar. 2010. DOI: 10.1109/amc.2010.5464027.
- [2] N. G. K. V. Shihabudheen and G. Dileep, “Applying h-infinity for stability control in two wheeled mobile manipulator”, *2015 International Conference on Soft Computing Techniques and Implementations- (ICSCTI)*, Oct. 2015. DOI: 10.1109/ICSCTI.2015.7489561.
- [3] J. Ito and T. Murakami, “Underactuated control for two-wheeled mobile robot with an arm using torque constraint conditions and disturbance observer”, *2023 IEEE 32nd International Symposium on Industrial Electronics (ISIE)*, Jun. 2023. DOI: 10.1109/ISIE51358.2023.10228153.
- [4] H. Kanazawa, K. Ishizaki, Y. Miyata, M. Nawa, N. Kato, and T. Murakami, “Model-based pitch angle compensation for center of gravity variation in underactuated system with an arm”, *2023 IEEE 32nd International Symposium on Industrial Electronics (ISIE)*, Jun. 2023. DOI: 10.1109/ISIE51358.2023.10228009.
- [5] IEEE, *Handle*, (accessed Nov.1, 2023): <https://robotsguide.com/robots/handle>.
- [6] F. I. for Material Flow-and-Logistics IML, *Evobot - the evolution of autonomous mobile robotic systems*, (Accessed Nov.1, 2023): [https://www.ilm.fraunhofer.de/en/fields\\_of\\_activity/material-flow-systems/iot-and-embedded-systems/evobot.html](https://www.ilm.fraunhofer.de/en/fields_of_activity/material-flow-systems/iot-and-embedded-systems/evobot.html).
- [7] Y. Nagatsu and H. Hashimoto, “Force control for vehicle robot with inverted two wheeled and stable travelling modes”, *IECON 2019 - 45th Annual Conference of the IEEE Industrial Electronics Society*, 2019. DOI: 10.1109/iecon.2019.8926672.
- [8] A. Gopinath and V. R. Jisha, “Gain scheduled lqr control of a two wheeled mobile robot with heavy payloads”, *2022 IEEE International Conference on Signal Processing, Informatics, Communication and Energy Systems ( SPICES)*, Mar. 2022. DOI: 10.1109/spices52834.2022.9774265.

- [9] V. Klemm and et al., “Ascento: A two-wheeled jumping robot”, *2019 International Conference on Robotics and Automation (ICRA)*, May 2019. DOI: 10.1109/icra.2019.8793792.
- [10] S. Wang and et al., “Balance control of a novel wheel-legged robot: Design and experiments”, *2021 IEEE International Conference on Robotics and Automation (ICRA)*, May 2021. DOI: 10.1109/icra48506.2021.9561579.
- [11] E. Ackerman, *Tencent's new wheeled robot flicks its tail to do backflips*, (Accessed Nov.1, 2023): <https://spectrum.ieee.org/tencents-new-wheeled-robot-flicks-its-tail-to-do-backflips>.
- [12] F. Raza, W. Zhu, and M. Hayashibe, “Balance stability augmentation for wheel-legged biped robot through arm acceleration control”, *IEEE Access*, Apr. 2021. DOI: 10.1109/access.2021.3071055.
- [13] X.-S. Gao, L. Yan, P. Zhao, N. Du, and S. Bu, “Inverse kinematics solution and analysis for multi-dof mobile manipulator”, *2022 IEEE 17th Conference on Industrial Electronics and Applications (ICIEA)*, Dec. 2022. DOI: 10.1109/ICIEA54703.2022.10006046.
- [14] S. S. Mathew and V. R. Jisha, “Tracking control of a mobile manipulator with external torque disturbances using computed torque control”, *2020 IEEE 17th India Council International Conference (INDICON)*, Dec. 2020. DOI: 10.1109/INDICON49873.2020.9342099.
- [15] N. Tan, Z. Zhu, and P. Yu, “Neural-network-based control of wheeled mobile manipulators with unknown kinematic models”, *2020 International Symposium on Autonomous Systems (ISAS)*, Dec. 2020. DOI: 10.1109/ISAS49493.2020.9378850.
- [16] E. Vollenweider, M. Bjelonic, V. Klemm, N. Rudin, J. Lee, and M. Hutter, “Advanced skills through multiple adversarial motion priors in reinforcement learning”, *2023 IEEE International Conference on Robotics and Automation (ICRA)*, May 2023. DOI: 10.1109/icra48891.2023.10160751.
- [17] C. Schwarke, V. Klemm, M. v. d. Boon, M. Bjelonic, and M. Hutter, “Curiosity-driven learning of joint locomotion and manipulation tasks”, in *Proceedings of The 7th Conference on Robot Learning*, J. Tan, M. Toussaint, and K. Darvish, Eds., ser. Proceedings of Machine Learning Research, vol. 229, PMLR, Jun. 2023, pp. 2594–2610. [Online]. Available: <https://proceedings.mlr.press/v229/schwarke23a.html>.
- [18] E. Sihite, A. Kalantari, R. Nemovi, A. Ramezani, and M. Gharib, “Multi-modal mobility morphobot (M4) with appendage repurposing for locomotion plasticity enhancement”, *Nature Communications*, vol. 14, no. 1, 2023. DOI: 10.1038/s41467-023-39018-y.
- [19] TOYO Automation Co., Ltd. “ETH2-17 Series, in TOYO Electric Actuator Total Catalog Vol. 16, pp. 14–19”. Accessed: 2025-07-02. (2025), [Online]. Available: [https://www.toyorobot.com/File/Fsrv\\_NoAuthority\\_Download/f25011613132034](https://www.toyorobot.com/File/Fsrv_NoAuthority_Download/f25011613132034).